A novel orthogonal anisotropic auxetic structure with enhanced auxeticity

Kang Gao [a], Zhiqiang Zou [b], Jiahui Liu [b], Zeyang Li [a], Zhangming Wu [a,*]

[a] School of Engineering, Cardiff University, The Parade, Cardiff CF24 3AA, UK
[b] Key Laboratory of Concrete and Prestressed Concrete Structures of the Ministry of Education, School of Civil Engineering, Southeast University, Nanjing, China

ARTICLE INFO

ABSTRACT

Auxetic structures have been utilized in various fields due to their unique deformation patterns and functional versatility. However, most research has focused on isotropic auxetic structures. Orthogonal anisotropic auxetic structures, which can exhibit a negative Poisson's ratio below -1 in a single direction, have not been thoroughly investigated, despite their unique applications in vascular stents, sensors, piezoelectric energy harvesters and many other fields. In this study, a novel orthogonal anisotropic auxetic structure with enhanced auxeticity (ASEA) was obtained through topology optimization using a modified SIMP method and an energy-based homogenization approach. Different initial design domains and varied topology optimization parameters were employed to mitigate the influence of optimization parameters on the final results and to discover more topological configurations. The Poisson's ratios of the obtained unit cells were calculated using the energy homogenization method. The unit cell with the minimum auxetic ratio was selected and simplified for subsequent parametric design and analysis. Subsequently, quasi-static compression tests and finite element simulations were conducted to investigate the deformation, energy absorption, and Poisson's ratio properties of the structure. The influence of structural parameters on the structural properties was thoroughly studied. Results show that the Poisson's ratio of the structure could reach -4 to -6 in the elastic stage and then decay rapidly to 0 with increasing strain. The mechanical properties of the structure are programmable by altering the structural parameters. This study provides a new approach to designing anisotropic auxetic structure with enhanced auxeticity.

1. Introduction

Mechanical metamaterials are a class of special artificially designed materials that achieve exceptional properties unattainable by conventional materials through the unique design of their geometric structure and distribution of constituent materials [1–4]. The development of additive manufacturing has made it feasible to fabricate structures with complex geometries [5,6]. Numerous studies have realized mechanical metamaterial with counterintuitive properties such as negative stiffness [7,8], zero stiffness [9,10], negative thermal expansion coefficient [11–13], zero thermal expansion coefficient [14,15], zero Poisson's ratio [16,17], and negative Poisson's ratio [18–21]. Among these, structures with negative Poisson's ratio, commonly known as auxetic structures, are one of the most extensively studied types of mechanical metamaterials. When auxetic structures are subjected to axial compression, they exhibit contraction in the transverse direction, and vice versa. This distinctive deformation mechanism endows auxetic structures with superior crashworthiness [22], improved fracture

toughness [23], and increased shear resistance [24]. However, most existing research focuses on designing isotropic negative Poisson's ratio structures that approach the lower bound (-1) [25–27], while studies on anisotropic structures with enhanced auxeticity (ASEA) remain limited.

Isotropic materials exhibit uniformity in all directions, with a theoretical Poisson's ratio limit ranging from -1 to 0.5. In contrast, anisotropic materials show different properties in different directions. According to the orthotropic constitutive law, thermodynamics predicts a general limit on Poisson's ratios within the linear and stable elastic regime: $0 \leq \nu_{ij}\nu_{ji} < 1$, where ν_{ij} and ν_{ji} are the Poisson's ratios in two orthogonal directions [28]. Therefore, anisotropic structures can achieve arbitrarily large positive or negative Poisson's ratios in a single direction, which makes them highly promising for a wide range of applications across various fields. Anisotropic auxetic structures can offer great axial stiffness and lateral deformation capabilities [29,30]. Vascular stents designed with highly anisotropic auxetic structures (Fig. 1(a)) exhibit excellent expansion deformation capabilities. These stents show significant radial contraction when axial pressure is applied

* Corresponding author.
E-mail address: wuz12@cardiff.ac.uk (Z. Wu).

and remain stable axially under radial pressure [31–33]. Auxetic structures exhibit exceptional energy absorption capabilities and have a high specific energy absorption capacity due to the unique deformation pattern [34]. Therefore, they can be used as fillers in energy-absorbing devices as shown in (Fig. 1(b). Because the Poisson's ratio of highly anisotropic auxetic structures can be less than -1, these structures can exhibit greater deformation in one direction when subjected to deformation in another direction, thus amplifying strain. Auxetic piezoelectric energy harvesters (see Fig. 1(c)) can simultaneously activate the d31 and d32 modes, thereby increasing the charge transfer pathways in the piezoelectric material and improving energy harvesting efficiency [35, 36]. The piezoelectric power output is related to the magnitude of stress in two directions; the greater the stress, the higher the power output. Thus, piezoelectric energy harvesters with enhanced auxeticity can generate greater stress perpendicular to the force direction, enhancing power output. As shown in Fig. 1(d), piezoresistive strain sensors with enhanced auxetic substrates can exhibit improved sensitivity, and the piezoresistive sensitivity of the sensor increases with the decrease in the substrate's Poisson's ratio [37,38].

Despite the promising applications of ASEA across various fields, research on their design methodologies and mechanical properties remains limited. In recent years, a variety of basic auxetic unit cells have been proposed, including chiral [39], arrow-head [40], re-entrant [41], star [42], and origami [43] structures. Many new auxetic structures were developed based on these unit cells. Zhang et al [44] studied the negative Poisson's ratio effect of re-entrant structures under tension, finding that their Poisson's ratio can reach as low as -4. Zhang et al [45] and Xu et al [46] replaced the inclined beams of re-entrant structures with cosine-shaped buckling beams and the auxeticity of the structure was improved by 28 %. Lu et al [41] combined star and circular shapes to enhance both the Young's modulus and auxeticity effect, achieving a minimum negative Poisson's ratio of -2.5 through structural parameter adjustments. Beyond these foundational auxetic structures, researchers have introduced more complex and novel auxetic structures inspired by biomimetic concepts. For instance, inspired by the shape of butterfly wings, Alomarah et al [47] proposed a new type of auxetic structure with two plateau stages and high specific energy absorption. Ma et al [48] developed lattice structures with a tunable Poisson's ratio based on the shape of a horseshoe. Zhang et al [49] studied the horseshoe lattice structures with different unit cells, and investigated the effect of the cell wall angle on the energy absorption and failure mechanisms. Chen et al

[50], inspired by hedgehog spines, invented a novel helmet design with excellent protective properties. Jiang et al [51] proposed a biomimetic self-similar negative Poisson's ratio structure with enhanced crashworthiness and energy absorption capacity according to the shape of the microstructure of coconut palm.

Although the approaches mentioned above can obtain novel and high-performance metamaterials, the structural topology and design space may be confined to a limited range. Topology optimization, which seeks the optimal distribution of material within a design domain, has demonstrated significant success in designing metamaterials with target or extreme properties subject to specific constraints [52]. Zheng et al [53] utilized the bi-directional evolutionary structural optimization (BESO) method and energy-based homogenization method (EBHM) to design mechanical metamaterials with auxetic properties. Gupta et al [54] designed multi-material auxetic structures based on topology optimization while considering stress constraints. Li et al [27] employed a discrete topology optimization method to achieve metamaterials with extreme isotropy and negative Poisson's ratio which is close to the lower bound -1. Auxetic mechanical metamaterials with gradually stiffer property were obtained through topology optimization and parametric optimization [55,56]. Most of the research mentioned above focuses on isotropic auxetic structures, and very few have investigated orthogonal anisotropic auxetic structures.

In this paper, a novel auxetic structure with enhanced auxeticity is developed. Topology optimization method is utilized to obtain the optimal topology of the structure with the objective of minimizing the structural Poisson's ratio. In order to explore more structural topologies with enhanced auxeticity, the topology optimization was carried out using different initial design domains and optimization parameters. The optimized structure with lowest negative Poisson's ratio was selected for further study. Axial compression tests and finite element analysis were carried out to investigate the deformation mechanism, Poisson's ratio and energy absorption properties of the structure under in-plane compression. Parametric analysis was carried out to investigate the effect of geometric parameters on the Poisson's ratio and compression performance of the structure.

2. Design methodology

In order to obtain the structural configuration with enhanced auxeticity, topology optimization methods were employed to find the
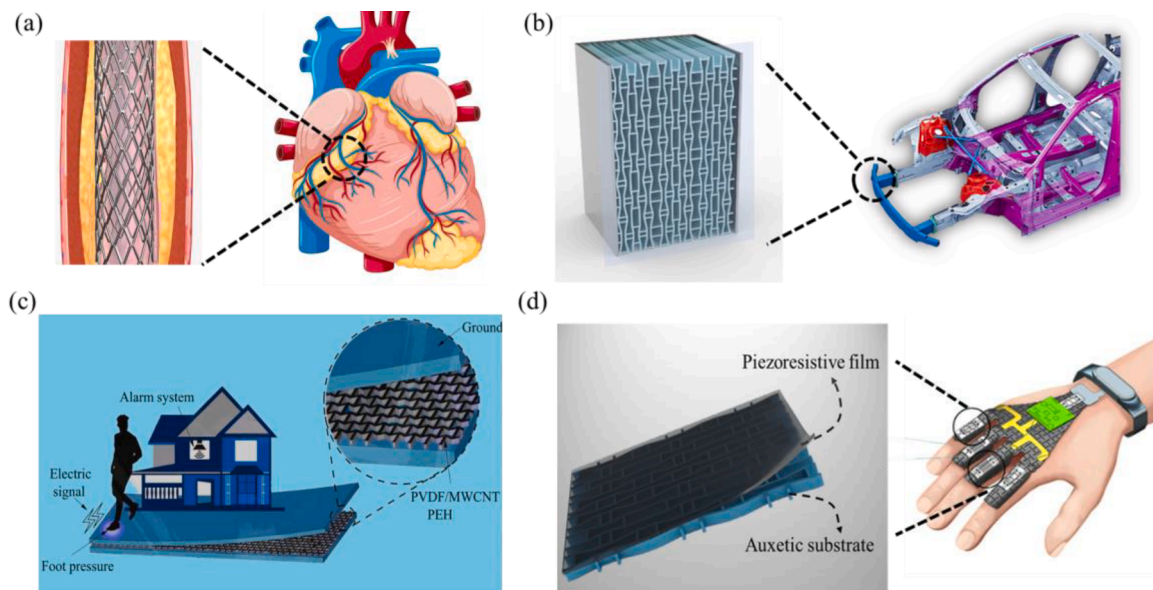
Fig. 1. The applications of anisotropic auxetic structures with enhanced negative Poisson's ratio. (a) Auxetic vascular stent. (b) Energy absorber. (c) Piezoelectric energy harvesters [35]. (d) High performance stretchable stain sensors.

optimal configuration. Different topology optimization parameters were employed to obtain a variety of topology configurations. The structural topology with minimum negative Poisson's ratio was selected and simplified for further research.

2.1. Topology optimization method

Topology optimization methods are often employed to discover optimal topologies that satisfy specific constraints. In this paper, topology optimization methods based on energy homogenization [57] and modified solid isotropic material with penalization (SIMP) method are used to obtain periodic unit cell with negative Poisson's ratio effect. Based on the homogenization theory, the effective uniform elasticity tensor of a periodic structure can be expressed in the following form [58]:

$$E_{ijkl}^H = \frac{1}{|Y|} \int_Y E_{pqrs} \left(\varepsilon_{pq}^{0(ij)} - \varepsilon_{pq}^{(ij)} \right) \left(\varepsilon_{rs}^{0(kl)} - \varepsilon_{rs}^{(kl)} \right) dV, \tag{1}$$

where Y denotes the area of the unit cell, E_{pqrs} is the locally varying stiffness tensor, $\varepsilon_{pq}^{0(ij)}$ is the applied macroscopic strain fields which induces the locally varying strain fields. In finite element analysis, the design domain is discretized into N finite elements, and Eq. (1) can be further calculated as follows

$$E_{ijkl}^H = \frac{1}{|V|} \sum_{e=1}^N \left(u_e^{A(ij)} \right)^T k_e u_e^{A(kl)}, \tag{2}$$

where $u_e^{A(kl)}$ are the element displacement solutions to the macro strain fields $\varepsilon_{pq}^{0(ij)}$ and k_e is the element stiffness matrix. The modified SIMP method [59] is used here and the element Young's modulus is defined as

$$E_e(\rho_e) = E_{min} + \rho_e^p (E_0 - E_{min}), \tag{3}$$

where E_0 is the Young's modulus of solid material and E_{min} is a very small Young's modulus assigned to void element to avoid singularity of the stiff matrix, ρ_e represents the element density, p is the penalty factor used to improve the stability of the algorithm. The mathematical formulation of the optimization problem is formulated as follows

$$\begin{aligned} &\min_\rho : g\left(E_{ijkl}^H(\rho) \right) \\ &s.t. : KU^{A(kl)} = F^{(kl)} \\ &: \sum_{e=1}^N v_e \rho_e \Big/ |Y| \le \vartheta \\ &: 0 \le \rho_e \le 1, e = 1, \dots, N \end{aligned} \tag{4}$$

where $g\left(E_{ijkl}^H(\rho) \right)$ is the optimization objective function based on the effective elasticity tensor as a function of the relative density ρ, K is the global stiffness matrix, $U^{A(kl)}$ and $F^{(kl)}$ are the global displacement vector and the external force vector for the test case (kl), respectively. ρ_e represents the element volume fraction and ϑ is the upper bound on the volume fraction. Based on the definition of Poisson's ratio, it can be determined as follows

$$\mu = \frac{E_{1122}}{E_{1111}}. \tag{5}$$

However, if the above formula is directly used as the optimization objective, the optimization process may be unstable [58]. Therefore, an additional bulk modulus constraint is added, and the final optimization objective function can be written as

$$g = E_{1122} - \beta^l (E_{1111} + E_{2222}), \tag{6}$$

where β is a fixed parameter and is defined as 0.8 in this paper and l is the iteration number. Using this optimization objective function, the optimizer initially focuses on maximizing both the horizontal and vertical stiffness of the material. As the optimization process continues, the optimizer then shifts its focus towards minimizing E_{1122} to achieve a negative Poisson's ratio. The sensitivity analysis can be calculated as

$$\frac{\partial g}{\partial \rho_e} = \frac{\partial E_{1122}}{\partial \rho_e} - \beta^l \left(\frac{\partial E_{1111}}{\partial \rho_e} + \frac{\partial E_{2222}}{\partial \rho_e} \right), \tag{7}$$

and the sensitivity for the homogenized elasticity tensor can be formulated as

$$\frac{\partial E_{ijkl}^H}{\partial \rho_e} = \frac{1}{|Y|} p \rho_e^{p-1} (E_0 - E_{min}) \left(\mathbf{u}_e^{A(ij)} \right)^T \mathbf{k}_0 \mathbf{u}_e^{A(kl)}. \tag{8}$$

The optimization parameters, such as the initial design domain, the penalization factor (p) and the filter radius (r), have significant impacts on the final design. Based on previous research [60], different initial design domain could lead to totally different final results. An increased number of holes signifies a more complex topology, resulting in a more intricate final structure, which could have better properties. Therefore, we employed ten distinct initial configurations of the design domain, as depicted in Fig. 2, to conduct comprehensive topology optimization studies aimed at expanding design space. These structures are uniaxially symmetric and were generated by varying the position and size of the holes. According to the study [57], different filter radius and penalization factor could result in different structures. Topology optimization with smaller filter radius can generate structures with richer details. A larger penalization factor accelerates algorithm convergence, producing clearer structures; however, it may also cause the algorithm to become trapped in local minima. Therefore, we selected a range of optimization parameters based on existing research and experience. The target density was varied from 0.1 to 0.7 in increments of 0.05, the filter radius ranged from 2 to 6 in steps of 1, and the penalization factor was set at 3, 5, and 7. After excluding non-convergent and redundant structures, a total of 841 distinct optimized topologies were obtained. Their corresponding Poisson's ratios and representative unit cell structures are depicted in Fig. 3. It can be observed that most optimized structures exhibit Poisson's ratios between 0 and -1, with only a few configurations demonstrating enhanced negative Poisson's ratio characteristics. This indicates that conducting extensive topology optimization with varied parameters can yield structures with extreme mechanical properties. Table 1 shows a series of optimized structural topologies with different optimization parameters. Some typical convergence curves during the optimization process are illustrated in Fig. 4, and the curve number corresponds to the optimization parameters and structures shown in Table 1. The iteration process of the structure with minimal Poisson's ratio is shown in Fig. 5. It can be seen that the optimized structures exhibit negative Poisson's ratio effects and possess diverse and complex topologies that are difficult to achieve through biomimetic design or intuition-based methods. It is noteworthy that structures 1–3 exhibit extreme negative Poisson's ratio effects (-15.434). The elasticity tensor matrices of these structures possess four independent components, and the Poisson's ratio is different along x- and y- directions. This reflects that these structures are orthotropic anisotropic structures with 2 symmetry axes, contrasting with the majority of studied configurations that exhibit orthogonally isotropic behavior. Further experiments and finite element analysis were conducted to study this unique structure comprehensively.

2.2. Design parameters

The obtained topology is further simplified to facilitate parametric analysis and improve manufacturability. Although additive manufacturing allows the fabrication of highly complex structures, intricate designs are challenging to analyze using simpler methods and are difficult to accurately print [61]. The structure shown in Fig. 6 (a) has non-uniform thickness, which significantly increases the complexity
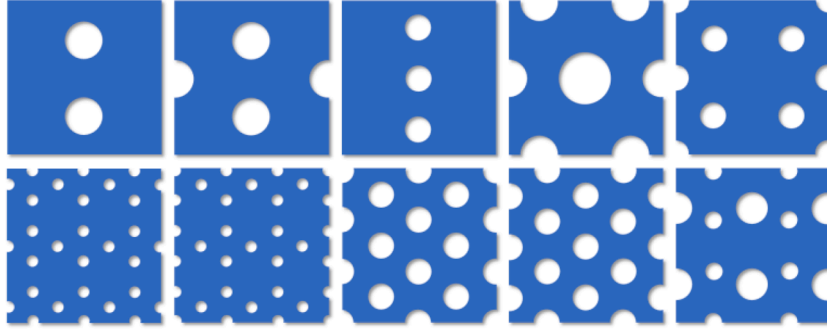
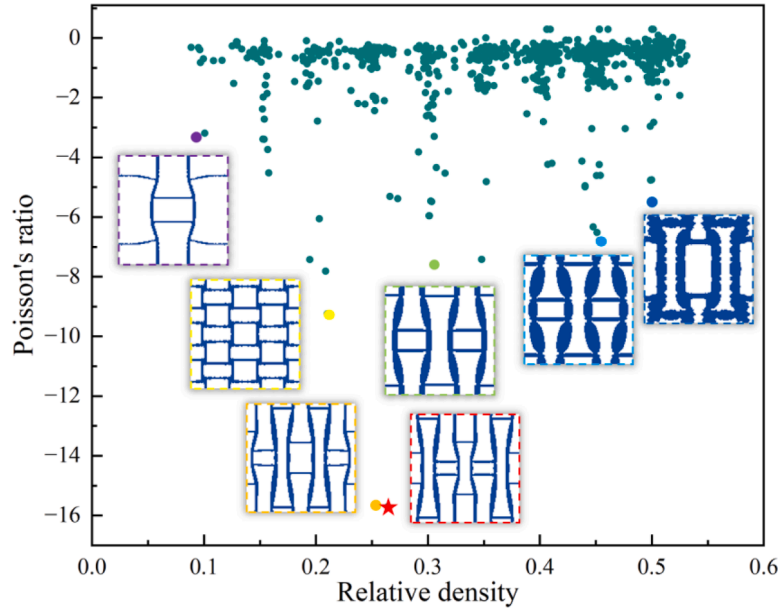**Fig. 2.** Selected configurations of initial design domain.

Fig. 3. The Poisson's ratio of the optimized structures with various initial design domain and optimization parameters. Some typical topologies are displayed.

of design analysis and manufacturing. Therefore, we adopt the simplified structure depicted in Fig. 6 (b), where the most significant modification is transforming the structure into one with uniform thickness.

The simplified unit cell resembles a combination formed by connecting two elongated re-entrant structures and one short, wide re-entrant structure with straight rods. The dimensions of the unit cell are defined $L = 30mm$ considering the printing precision. The primary design parameters include the thickness of the cell walls t, the width of sub-structures $a1, a2$, the length of inclined and vertical rods in the elongated sub-structure $b1,b2,b3$, the length of inclined and vertical rods in the short, wide sub-structure $c1, c2, c3$, the angle of inclined rods in both sub-structures $\alpha1, \alpha2$, and the distance from the center of the elongated substructure to the left boundary of the unit cell d. To further simplify the parameters of the unit cell, we assume $a1 = a2 = a, b1 = b2 = b3 = b$, $c1 = c2 = c3 = c$, $\alpha1 = \alpha2 = \alpha$, $d = \frac{L}{6}$, resulting in a centrosymmetric unit cell. The lengths of the upper and lower connecting rods in the elongated sub-structure are denoted as m_1 and m_2, and can be calculated as Eq. (9), while the lengths of the upper and lower connecting rods in the short, wide sub-structure are denoted as n_1 and n_2, and can be derived by Eq. (10). The length of the left connecting rod (p) can be calculated by Eq. (11), and the length of the right connecting rod (q) can be derived by Eq. (12). Furthermore, the relative density of the structure (ρ^*) can be estimated through the lengths and thickness of various cell walls, as provided in Eq. (13). It should be noted that the width of sub-structures has no impact on the relative density.

$$m_1 = m_2 = m = \frac{L - 3b}{2} \tag{9}$$

$$n_1 = n_2 = n = \frac{L - 3c}{2} \tag{10}$$

$$p = d - \frac{a}{2} + \frac{b}{\tan\alpha} \tag{11}$$

$$q = \frac{L}{3} - a + \frac{(b + c)}{\tan\alpha} \tag{12}$$

$$\rho^* = \frac{t \times \left(14L - 20b - 10c + \frac{8b}{\sin\alpha} + \frac{8b}{\tan\alpha} + \frac{4c}{\sin\alpha} + \frac{4c}{\tan\alpha}\right)}{L^2} \tag{13}$$

3. Experiment and numerical methods

In this section, the experiment and finite element analysis (FEA) are conducted to study the structure's deformation pattern and mechanical responses.
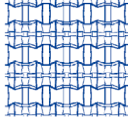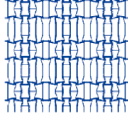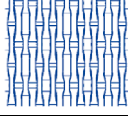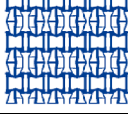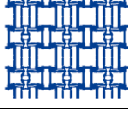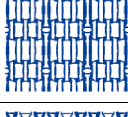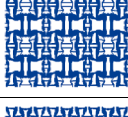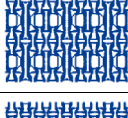
3.1. Experimental setup

The novel structures were fabricated through 3D printing with Poly lactic acid (PLA) material. Three dog-bone were fabricated using the

Table 1

Optimal microstructures and effective elasticity matrices of optimized structures for various target density, penalization factor and filter radius.

| No.	Target density	p	R	Unit cell	3 x 3 Array	Effective Property $\mathbf{D^H}$	ν_{12}, ν_{21}
1-1	25%	3	2			$\begin{bmatrix} 13.092 & -8.838 & 0 \\ -8.838 & 10.548 & 0 \\ 0 & 0 & 0.121 \end{bmatrix}$	-0.6751 -0.8379
1-2			4			$\begin{bmatrix} 5.626 & -6.015 & 0 \\ -6.015 & 14.881 & 0 \\ 0 & 0 & 0.081 \end{bmatrix}$	-1.0691 -0.4042
1-3		5	2			$\begin{bmatrix} 0.117 & -1.801 & 0 \\ -1.801 & 38.847 & 0 \\ 0 & 0 & 0.066 \end{bmatrix}$	**-15.434** -0.0464
1-4			4	Not convergent	\	\	\
2-1	40%	3	2			$\begin{bmatrix} 17.855 & -13.409 & 0 \\ -13.409 & 19.205 & 0 \\ 0 & 0 & 0.510 \end{bmatrix}$	-0.7510 -0.6982
2-2			4			$\begin{bmatrix} 16.730 & -13.118 & 0 \\ -13.118 & 25.174 & 0 \\ 0 & 0 & 0.760 \end{bmatrix}$	-0.7841 -0.5211
2-3		5	2			$\begin{bmatrix} 17.274 & -13.118 & 0 \\ -13.118 & 24.033 & 0 \\ 0 & 0 & 0.664 \end{bmatrix}$	-0.7074 -0.5085
2-4			4			$\begin{bmatrix} 2.549 & -7.394 & 0 \\ -7.394 & 52.156 & 0 \\ 0 & 0 & 0.409 \end{bmatrix}$	-2.9013 -0.1418
3-1	55%	3	2			$\begin{bmatrix} 21.754 & -16.631 & 0 \\ -16.631 & 30.975 & 0 \\ 0 & 0 & 2.238 \end{bmatrix}$	-0.7645 -0.5369
3-2			4			$\begin{bmatrix} 4.108 & -10.003 & 0 \\ -10.003 & 58.759 & 0 \\ 0 & 0 & 1.622 \end{bmatrix}$	-2.4348 -0.1702
3-3		5	2			$\begin{bmatrix} 11.245 & -15.347 & 0 \\ -15.347 & 47.696 & 0 \\ 0 & 0 & 2.246 \end{bmatrix}$	-1.3648 -0.3218
3-4			4			$\begin{bmatrix} 27.030 & -9.133 & 0 \\ -9.133 & 50.085 & 0 \\ 0 & 0 & 2.326 \end{bmatrix}$	-0.3379 -0.1823
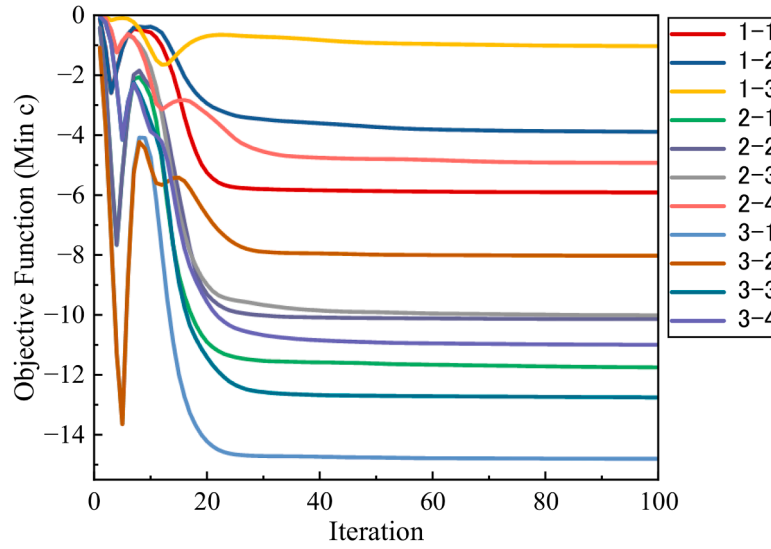
Fig. 4. The iterative curve of microstructures for different optimization parameters. The number corresponds to the optimization parameters and structures shown in Table 1.
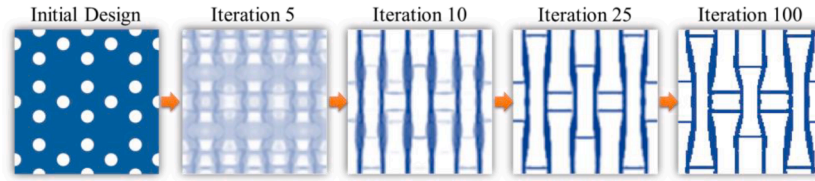
Fig. 5. Initial design domain and iteration process.
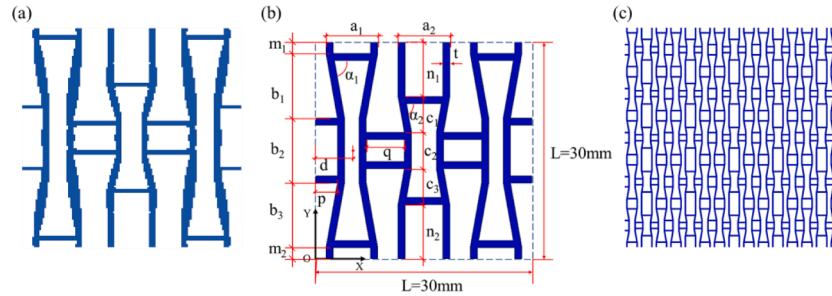
Fig. 6. Simplification and design parameters of novel auxetic structures. (a) Original optimized topology. (b) Simplified unit cell topology with design parameters. (c) 5 × 5 array of the unit cells.

same base material to assess the material property. The uniaxial tensile test was conducted using Instron 3367 testing machine and the stress-strain curves are shown in Fig. 7. The obtained material property is presented in Table 2. As shown in Fig. 8 quasi-static uniaxial compression tests were conducted on the novel structures using SHT4605 testing machine, with a loading speed of 2 mm/min. The samples contained 5 × 5 unit cells in-plane and had an out-of-plane length of 40 mm to prevent buckling during compression. The designed structural parameters were: $a = 7.2mm$, $b = 9.0mm$, $c = 5mm$, $\alpha = 80°$, and $t = 1mm$. A digital camera was used to capture the deformation process during the experiment.

3.2. Finite element model

Abaqus/Explicit was used for finite element analysis in this study. A schematic diagram of the finite element model is shown in Fig. 9(a). The structure is placed between two rigid plates to simulate the fixed and compression platforms of the experiment. The top plate was applied a downward displacement and the bottom rigid plate is fixed. The model is meshed using 8-node brick element with reduced integration (C3D8R). All surfaces are modeled with general contact interaction, with tangential behavior modeled using a penalty method and a friction coefficient of 0.4, and normal behavior modeled as hard contact. A mesh sensitivity analysis was conducted to select the optimal mesh size, as shown in Fig. 9(b), and a final average mesh size of 0.4 mm was chosen for the model. Additionally, to calculate the structure's negative Poisson's ratio, 16 nodes (a-p) were identified in the middle region of the structure, and the lateral and vertical displacements of these nodes were tracked during the computation. Then, Poisson's ratio can be calculated with the formula shown in Eq. (14) to Eq. (16):

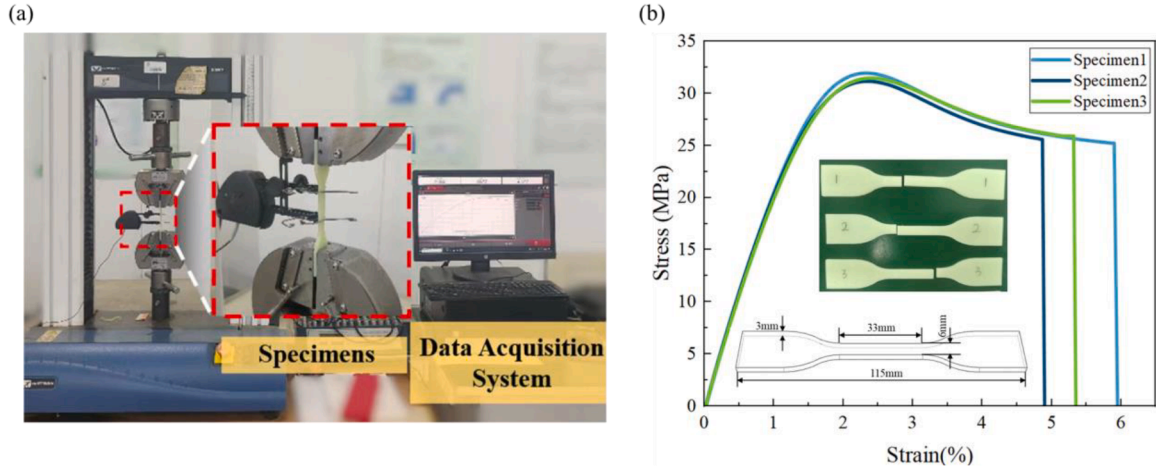$$\nu = -\frac{\varepsilon_x}{\varepsilon_y}, \tag{14}$$

Fig. 7. (a) Experimental setup of structures; (b) Stress-strain curve of base material and geometric parameters of dog-bone-shaped specimen.

Table 2
Specific physical and mechanical properties of PLA.

Material	Elastic modulus (MPa)	Poisson's ratio	Density (g/cm^3)	Yield stress (MPa)
PLA	2400	0.42	1.13	31

$$\varepsilon_x = \frac{\varepsilon_{\mathrm{af}} + \varepsilon_{\mathrm{pg}} + \varepsilon_{\mathrm{oh}} + \varepsilon_{ni}}{4}, \tag{15}$$

$$\varepsilon_y = \frac{\varepsilon_{\mathrm{an}} + \varepsilon_{bm} + \varepsilon_{ci} + \varepsilon_{dh} + \varepsilon_{ej} + \varepsilon_{fi}}{6}, \tag{16}$$

where ε_{af} represents the strain between node a and node f.

4. Results and discussion

4.1. Mechanical responses and deformation mode

Energy absorption indicators are commonly used to evaluate the mechanical properties of honeycomb structures [61]. These indicators primarily include plateau stress (σ_p), densification strain (ε_d) energy absorption (EA), and specific energy absorption (SEA). Plateau stress reflects the average stress experienced by the structure before reaching densification strain during compression, and is defined as:

$$\sigma_p = \frac{\int_0^{\varepsilon_d} \sigma(\varepsilon)d\varepsilon}{\varepsilon_d} \tag{17}$$

where ε_d is the densification strain and is usually determined by the highest point of the energy absorption efficiency curve. The energy absorption efficiency (η) is defined as the ratio of the energy absorbed by the porous structure to the nominal stress and is calculated as

$$\eta(\varepsilon) = \frac{\int_0^{\varepsilon} \sigma(\varepsilon)d\varepsilon}{\sigma(\varepsilon)} \tag{18}$$

where ε is the nominal strain and σ is the nominal stress. The energy absorption (EA) is the energy absorbed by the structure before the densification strain, and is defined as follows:

$$EA = \int_0^{\delta} F(x)dx \tag{19}$$

where $F(x)$ is the compression force, x is the compression displacement, and δ is the displacement corresponding to the densification strain. The specific energy absorption (SEA) is the energy absorbed per unit mass, and is defined as:

$$SEA = \frac{EA}{M} \tag{20}$$

where M is the total mass of the structure.

Fig. 10 shows the stress-strain responses obtained from both experiments and FEA. The entire deformation process can be divided into three distinct stages: elastic stage, plateau stage, and densification stage. The elastic stage is defined as the linear region before the initial peak stress, while the plateau stage is defined as the region between the peak stress strain and the densification strain. The region after the densification strain is referred to as the densification stage. The stress-strain and energy absorption efficiency curves from the experiments and FEA
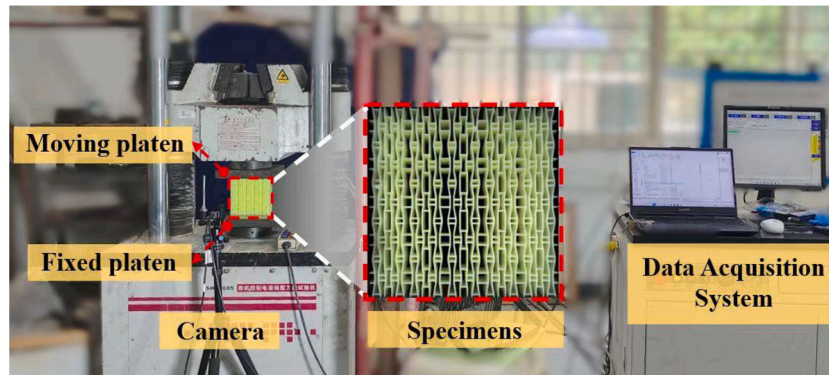

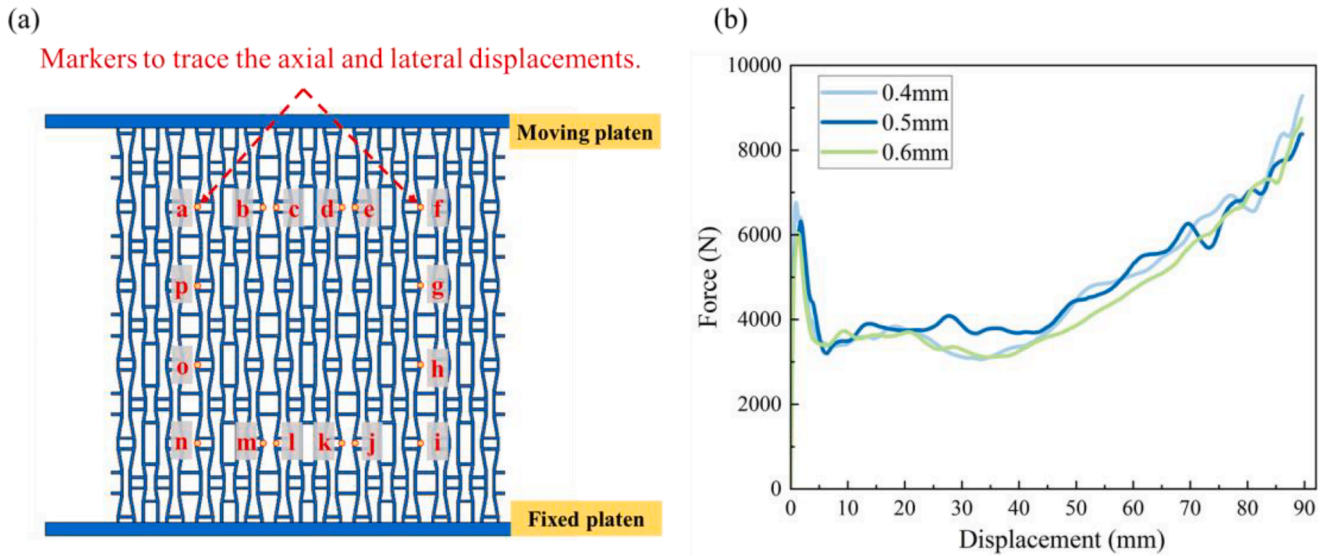**Fig. 8.** Set up of the quasi-static compression experiment.

Fig. 9. (a) Finite element model and displacement tracking points (b) Mesh sensitivity analysis.
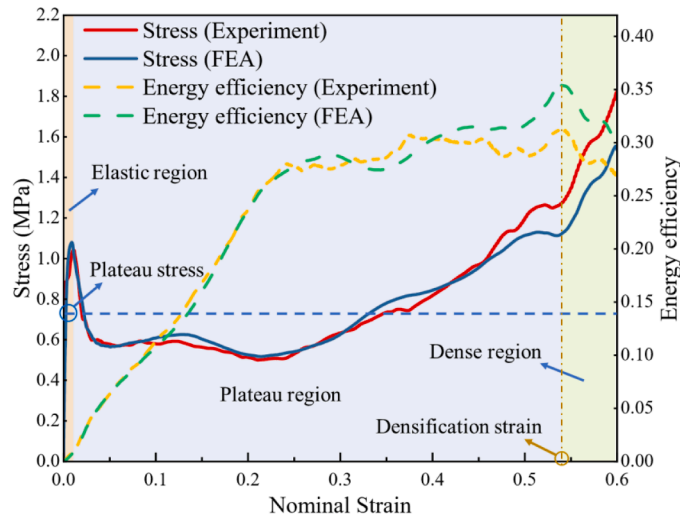

Fig. 10. Comparison of stress-strain curve and energy absorption efficiency curve of experiments and numerical simulation.

exhibit good agreement.

Table 3 compares the calculated values of plateau stress, densification strain, EA, and SEA which are very close, indicating that the developed finite element model is accurate and capable of providing reliable results for subsequent parametric analysis.

Fig. 11 compares the deformation processes from the experiment and the FEA model, with the compression displacement up to 90 mm, corresponding to a nominal axial strain of 0.6. The deformation process of the structure can also be divided into three stages: elastic stage, plateau stage, and densification stage. During the initial elastic stage, the deformation is elastic and reversible and the nominal stress increases linearly. Meanwhile, significant contraction occurs in the middle part of the structure, demonstrating a distinct negative Poisson's ratio behavior.

Table 3
Comparison of energy index of experiments and numerical simulation.

	σ_p(MPa)	ε_d	EA(J)	SEA(J/g)
Experiment	0.739	0.543	361.2	1.274
FEA	0.737	0.542	359.8	1.269

As the strain increases, some of the longer inclined ligaments begin to experience local buckling and the cell walls of the structure start to contact with each other. The nominal stress drops rapidly at this stage. Subsequently, it enters the plateau stage, during which numerous plastic hinges form in the central region, leading to overall buckling and instability. As the compressive displacement increases, the structure begins to rotate around these plastic hinges, and continuous contact occurs between the cell walls, forming two distinct shear bands. The deformation of the structure is in the shape of "S", during which the plateau stress slightly increases. Subsequently, the two shear bands become connected, buckling then occurs at the ends of the structure, accompanied by the formation of plastic hinges, and the ends begin to rotate around these hinges. As the structure is further compressed, more and more parts of the structures contact with each other. The stress continues to rise, while the rate of increase in energy absorption efficiency gradually decreases. Finally, a peak of the energy absorption efficiency is reached, indicating the transition to the densification stage. The structure is considered to be compacted at this stage, because the stress grows steeply and it can hardly contribute to further energy absorption.

Fig. 12(b) shows the deformation of the unit cell located in the center of the structure throughout the compression process. At a global strain of 0.0067, the structure is in the elastic stage, and the unit cell undergoes elastic deformation. Significant lateral deformation can be observed in the elongated substructures on both sides, while the lateral deformation in the central substructure is relatively small. When the strain reaches 0.0129, the lateral deformation of the substructures on both sides continues to increase, causing contact in the rod, at which point the Poisson's ratio of the entire structure reaches its minimum. Subsequently, the unit cell enters the plastic stage, buckling occurs in the rod, and simultaneously, the entire unit cell begins to rotate, leading to an increase in Poisson's ratio for the whole structure. As strain increases, the unit cell continues to rotate and gradually crushes. When strain reaches 0.6, most parts of the unit cell begin to contact each other and become densely crushed, and the entire structure reached the dense stage. Fig. 12 (a) compares the external contours of the unit cell at strains of 0, 0.0067, and 0.0129; it can be observed that the lateral contraction deformation of the unit cell is significantly greater than its vertical compressive deformation, confirming that the negative Poisson's ratio of the structure is very small. As shown in Fig. 13(d), during its initial elastic stage, negative Poisson's ratio of the structure continuously decreases until reaching a minimum and then gradually increases until stabilization; this is consistent with what was observed for unit cell
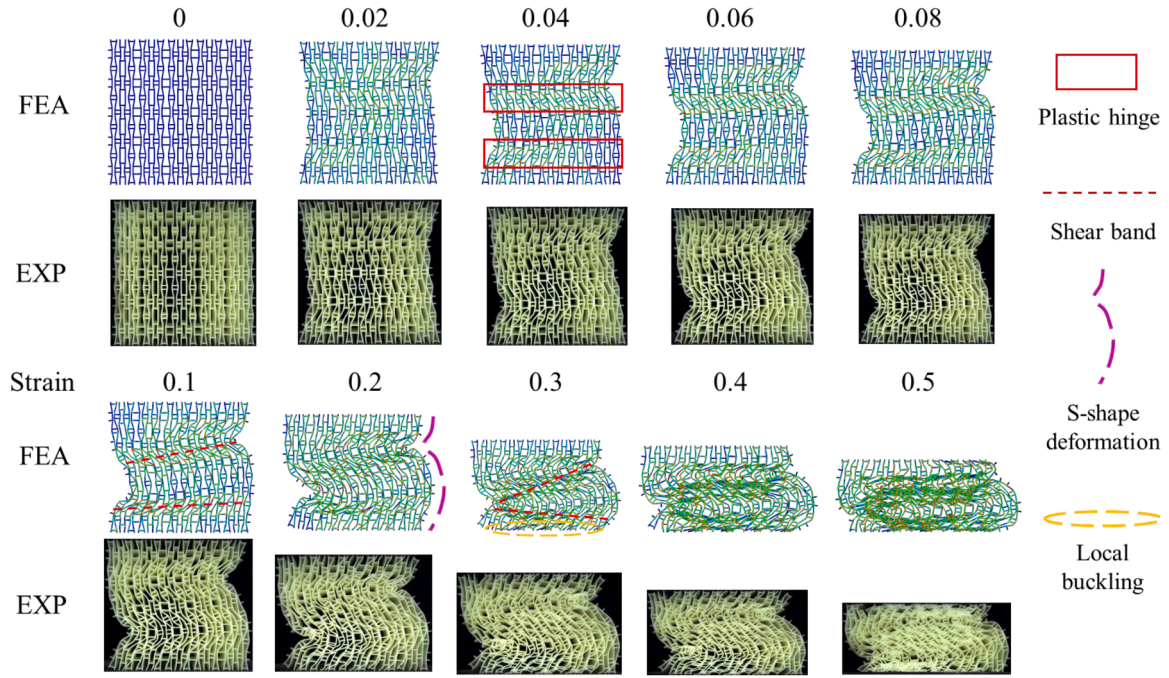
Fig. 11. Comparison of deformation process of experiments and numerical simulation.
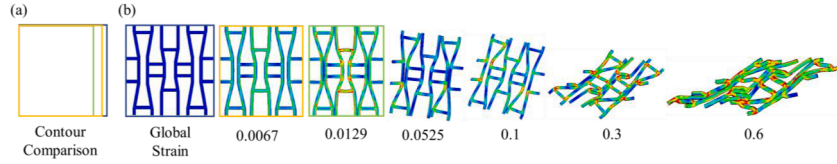

Fig. 12. (a) Comparison of contour at elastic stage. (b)The deformation of the unit cell at the middle position.

deformation. It can be concluded that during this initial elastic stage, a small negative Poisson's ratio in structures is caused by inherent negative Poisson's ratio effects of individual unit cells; thereafter, an increasing negative Poisson's ratio results from structural buckling and rotation.

4.2. Parametric analysis

In this section, the parametric analyses are carried out utilizing the validated finite element model to investigate the effect of structural parameters on the structural deformation, energy absorption, and Poisson's ratio.

4.2.1. Effect of cell wall thickness (t)

The compressive stress-strain response curves of structures with different cell wall thicknesses (t), are shown in Fig. 13 (a). The other geometric parameters are set as: $a = 7.2mm$, $b = 8.0mm, \alpha = 80°$. The initial peak stress and compressive stress increase with increasing t. As shown in Fig. 13 (b), the plateau stress increases monotonically as t increases, while the densification strain decreases monotonically with increasing t. EA and SEA prior to densification strain are presented in Fig. 13 (c). EA increases monotonically as t increases, which is due to the greater stress response of the structure with larger t. However, SEA first increases and then decreases with increasing t, reaching a peak at $t = 1.1$ mm. When $t > 1.2$ mm, SEA decreases because the mass of the structure also increases with t, and the structure becomes more prone to entering the densification stage. Fig. 13 (d) compares the Poisson's ratio curves of auxetic structures with different cell wall thicknesses. The minimum Poisson's ratio ranges between -4 and -6. It should be noted that as the

structure is derived from a simplified configuration, the Poisson's ratio is higher than the optimized structure calculated using the homogeneous method, as shown in Table 1. It can be observed that, as t decreases, the minimum negative Poisson's ratio of the structure becomes smaller. This is because a larger t results in greater lateral constraint forces within the structure, thereby reducing lateral deformation. Fig. 14 illustrates the deformation process of structures with different cell wall thicknesses. It can be seen that for $t = 0.8mm - 1.0mm$, at a strain of 0.2, two shear bands appear in the middle of the structure, which then gradually propagate throughout the structure as compression continues. For $t = 1.1$ mm, only one shear band appears at a strain of 0.2, and a second shear band forms at a strain of 0.3 before the structure enters the densification stage. For $t = 1.2$ mm and $t = 1.3$ mm, no distinct shear bands are observed, and the structure exhibits overall buckling deformation. This indicates that as the cell wall thickness increases, the structure's ability to resist local buckling deformation also strengthens.

4.2.2. Effect of cell wall angle (α)

Fig. 15 presents the compressive response of structures with different cell wall angles (α). The other geometric parameters are set as: $a = 7.2mm$, $b = 8.0mm, t = 1.0mm$. Smaller values of α lead to overlapping cell walls, so we selected $\alpha = 75° \sim 85°$ for further analysis. As shown in Fig. 15 (a), as α increases, the elastic stage of the structure becomes longer. This is because larger α increases the distance between cell walls, resulting in later contact between them and delaying the onset of buckling.

When α is greater than 80°, the initial plateau stress of the structure is high. This phenomenon arises because the inclined cell walls align more closely with the principal compressive stress direction, leading to
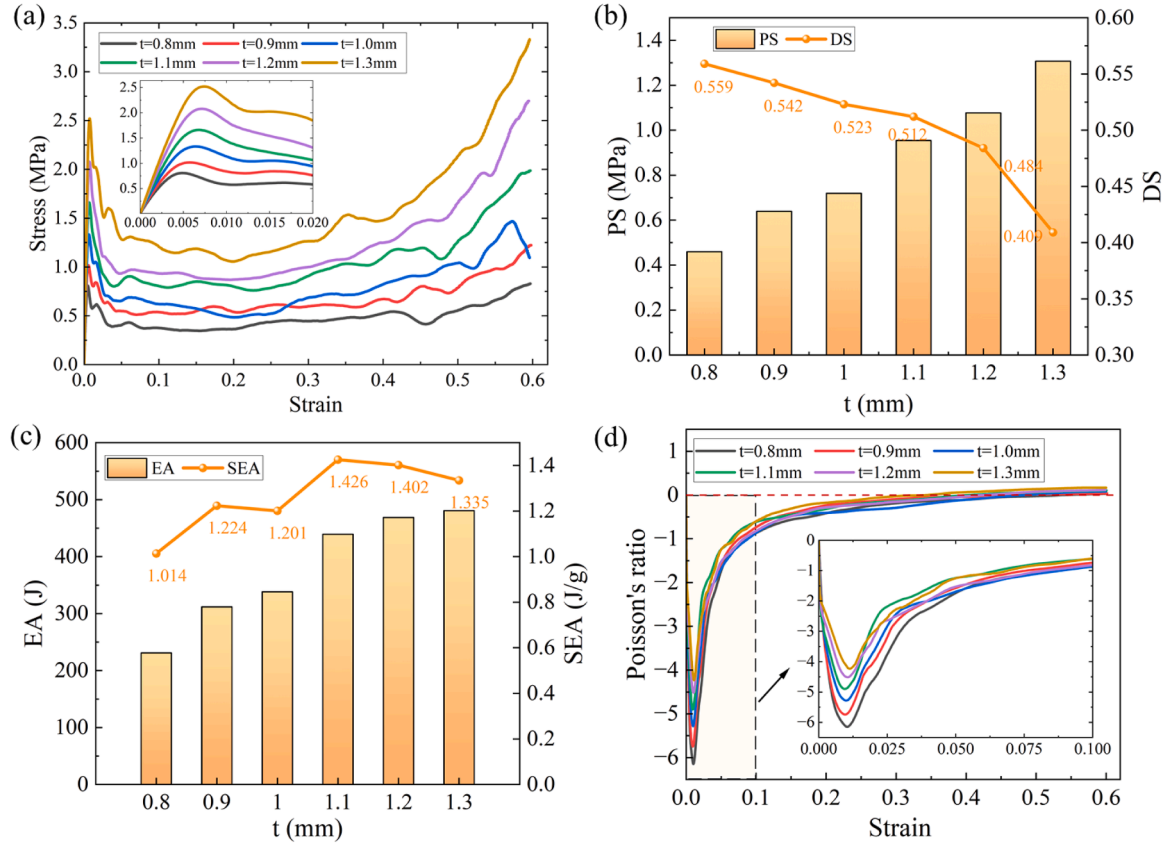
Fig. 13. Compression responses of structures with different *t*. (a) Stress-strain curves (b) Plateau stress (PS) and densification strain (DS) values.(c) Energy absorption (EA) and specific energy absorption (SEA) values. (d) Poisson's ratio curves.
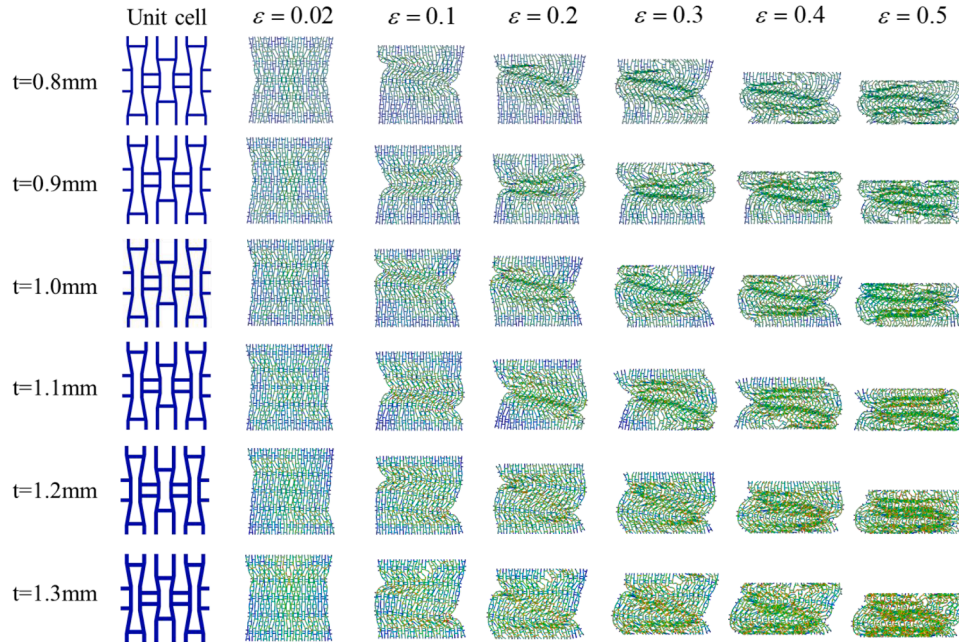
Fig. 14. The configuration of unit cell and deformation process of structures with different *t*.

stress concentrations at specific nodes. As shown in Fig. 16, this stress state triggers the formation of two lateral parallel shear bands during the early plateau stage. These localized densification bands enhance the overall stiffness through two mechanisms: (1) the reorientation of struts within the bands creates a load-redistribution path that resists further collapse, and (2) the strain energy is preferentially dissipated through progressive buckling of struts along these bands rather than random plastic deformation. When $\alpha = 80°$, two continuous inclined shear bands form in the central region due to symmetric stress distribution, enabling more uniform energy dissipation. In contrast, when $\alpha < 80°$, the lower
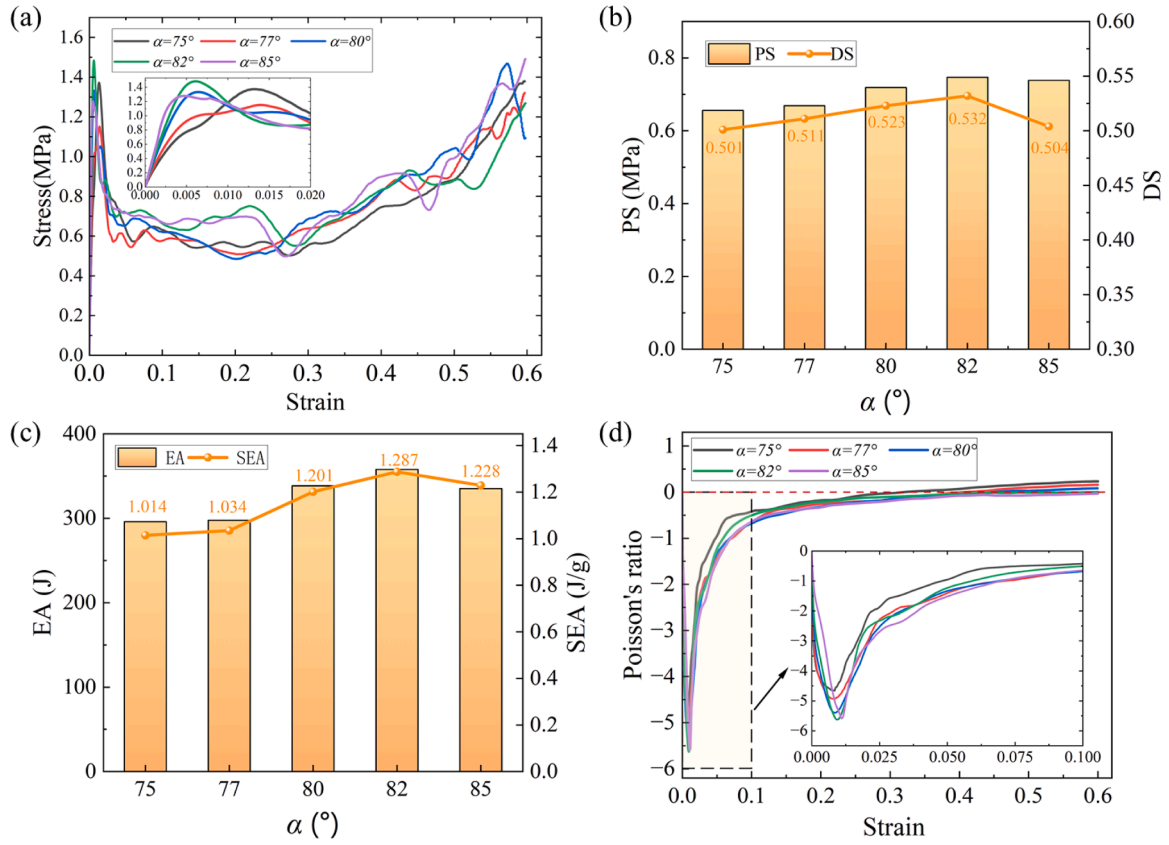
Fig. 15. Compression responses of structures with different α. (a) Stress-strain curves (b) Plateau stress (PS) and densification strain (DS) values (c) Energy absorption (EA) and specific energy absorption (SEA) values. (d) Poisson's ratio curves.
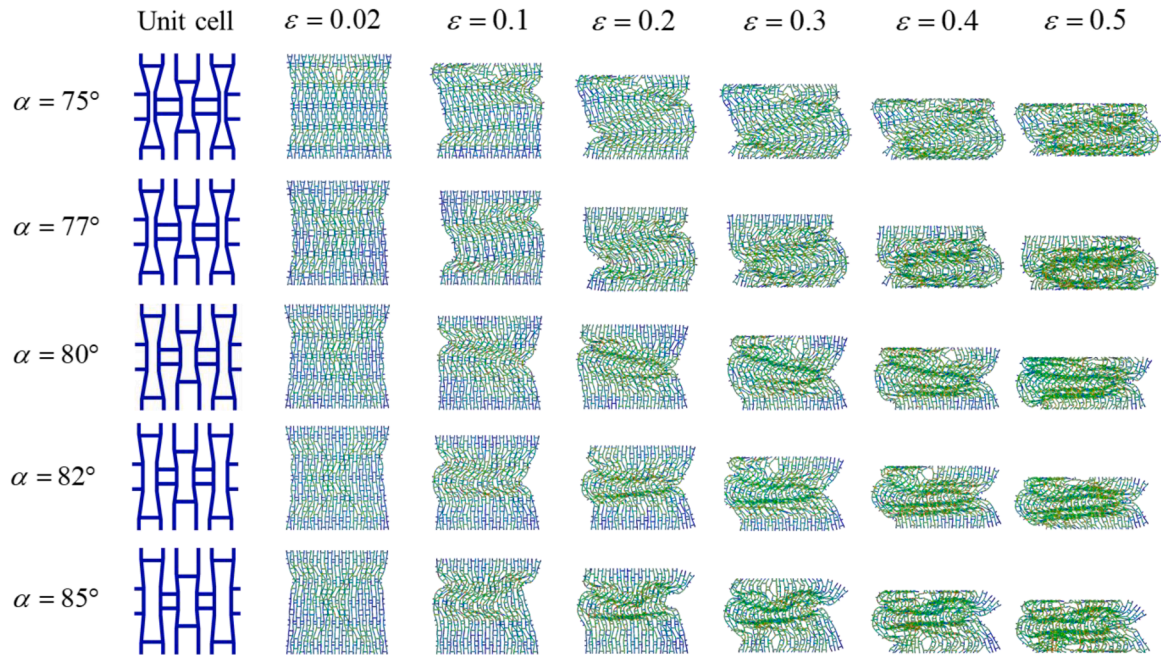

Fig. 16. The configuration of unit cell and deformation process of structures with different α.

cell wall inclination reduces stress localization, resulting in plastic deformation without distinct shear band formation and lower plateau stress. The energy absorption (EA) and specific energy absorption (SEA) initially increase and then decrease, reaching a peak at $\alpha = 82°$. Notably, according to Eq. (13), increasing α reduces the structural mass, but EA still increases, indicating that α has a significant influence on the energy absorption performance of the structure. Fig. 15 (d) shows the influence of α on the Poisson's ratio of the structure. It can be observed that as α increases, the minimum negative Poisson's ratio decreases, and the strain at which the minimum negative Poisson's ratio is reached

becomes larger.

4.2.3. Effect of sub-structure height (b)

Fig. 17 illustrates the compressive stress response of structures with varying sub-structure heights (*b*). The other geometric parameters are set as: $a = 7.2 mm, \alpha = 80°, t = 1.0 mm$. It can be observed that as *b* increases, the elastic modulus of the structure decreases, and the elastic stage becomes shorter. This is because larger values of *b* make the structure more susceptible to buckling. The densification strain initially decreases and then increases, which is related to the deformation mode of the structure. As shown in Fig. 18, when *b* is less than 7.0 mm, the vertical struts are relatively long and destabilizes before the sub auxetic structures. This results in the formation of multiple transverse shear bands in the middle region of the structure, enabling more comprehensive deformation. When *b* is greater than 7.0 mm, the sub auxetic structures are more likely to destabilize, primarily forming inclined shear bands that lead to extensive compression. However, when *b* = 7.0 mm, the structure exhibits a mixed deformation mode, preventing it from being fully compressed. EA and SEA both reach the peak when *b* = 6.0 mm and 8.5 mm. As shown in Fig. 17(d), the initial peak Poisson's ratio decreases as *b* increases.

4.2.4. Effect of sub-structure width (a)

The compressive stress-strain response curves of structures with different sub-structure width (*a*), are shown in Fig. 19(a). The other geometric parameters are set as: $b = 8.0 mm, \alpha = 80°, t = 1.0 mm$. Overall, the variation of *a* has a limited impact on the initial peak stress and compressive stress. When *a* = 9.0 mm, the initial peak stress significantly increases, exceeding 1.6 MPa, as shown in Fig. 1. (b). With the increase of *a*, the plateau stress fluctuates but remains stable between 0.6 and 0.75 MPa, indicating that *a* does not have a significant influence on the plateau stress. However, the densification strain

generally increases with increasing *a*, but it drops sharply to a minimum value of 0.45 when *a* = 8 mm. Fig. 19(c) presents the energy absorption (EA) and specific energy absorption (SEA) before the densification strain. Both EA and SEA initially increase, then decrease, and increase again with increasing *a*, reaching their minimum values at *a* = 8 mm and peaking at *a* = 9 mm. As shown in Fig. 19(d), the minimum Poisson's ratio decreases with the increase of *a*. Fig. 20 illustrates the deformation process of structures with different sub-structure width. It can be seen that for *a* = 7.5–9.0 mm, two shear bands appear in the middle of the structure at a strain of 0.2, and these shear bands gradually propagate throughout the structure as compression continues. For *a* = 7.0 mm, no distinct shear bands are observed at a strain of 0.2, but two shear bands form at a strain of 0.3. For *a* = 6.0 mm and *a* = 6.5 mm, no obvious shear bands are observed, and the structures exhibit overall buckling deformation. This indicates that as the substructure width increases, the structure's ability to resist local buckling deformation also strengthens.

4.2.5. Effect of sub-structure length (c)

The compressive stress-strain response curves of structures with different sub-structure height (*c*), are shown in Fig. 21(a). The other geometric parameters are set as: $a = 7.2 mm, b = 8.0 mm, \alpha = 80°, t = 1.0 mm$. Generally, the variation of *c* has a limited impact on the initial peak stress and compressive stress. As shown in Fig. 21(b), with the increase of *c*, the plateau stress fluctuates between 0.7 and 0.8 MPa, and the densification strain varies between 0.50 and 0.56, indicating that *c* does not significantly affect the plateau stress or densification strain. Fig. 21(c) presents the energy absorption (EA) and specific energy absorption (SEA) before the densification strain. As *c* increases, EA fluctuates between 300 and 400 J, and SEA varies between 1.2 and 1.4 J/g. Neither shows a clear trend, suggesting that *c* has no significant effect on EA or SEA. From Fig. 21(d), it can be seen that as *c* increases, the minimum negative Poisson's ratio decreases, and the strain required to

Fig. 17. Compression responses of structures with different *b*. (a) Stress-strain curves (b) Plateau stress (PS) and densification strain (DS) values. (c) Energy absorption (EA) and specific energy absorption (SEA) values. (d) Poisson's ratio curves.

Fig. 18. The configuration of unit cell and deformation process of structures with different sub-structure height *b*.

Fig. 19. Compression responses of structures with different a. (a) Stress-strain curves (b) Plateau stress (PS) and densification strain (DS) values. (c) Energy absorption (EA) and specific energy absorption (SEA) values. (d) Poisson's ratio curves.

Fig. 20. The configuration of unit cell and deformation process of structures with different sub-structure width *a*.
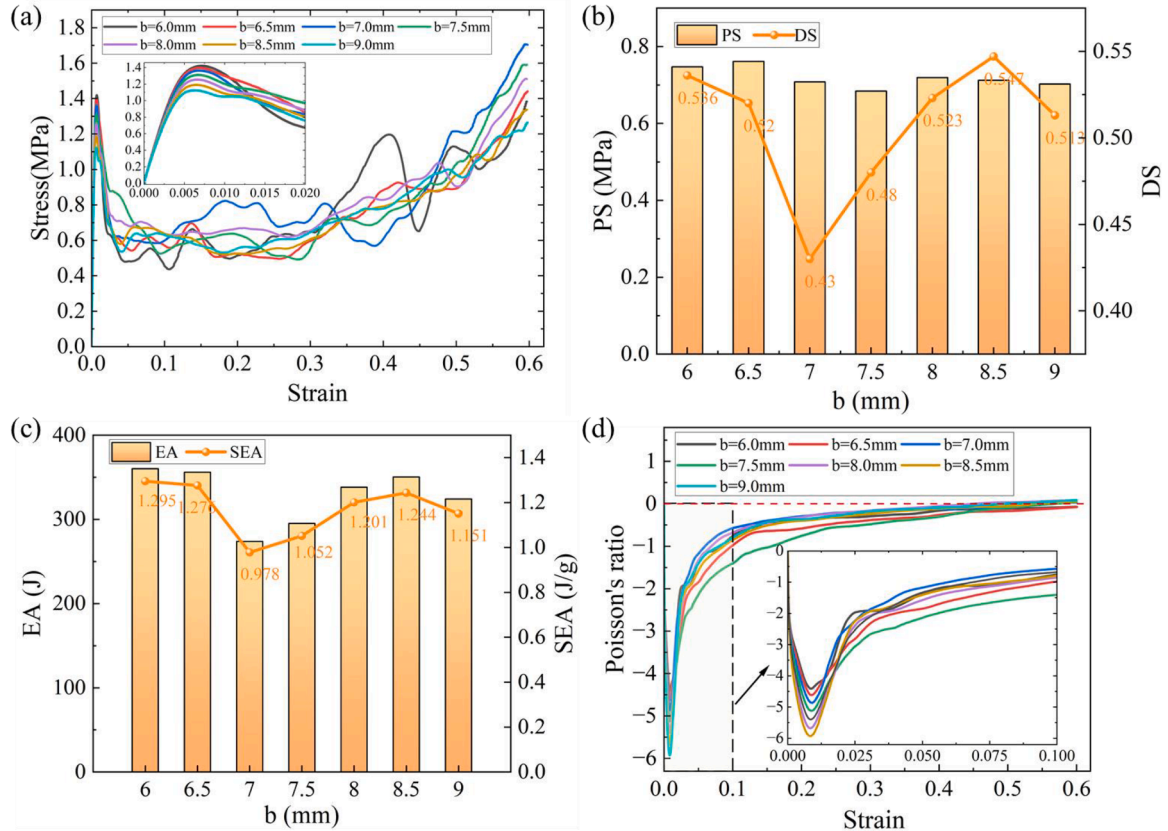

Fig. 21. Compression responses of structures with different *c*. (a) Stress-strain curves (b) Plateau stress (PS) and densification strain (DS) values. (c) Energy absorption (EA) and specific energy absorption (SEA) values. (d) Poisson's ratio curves.
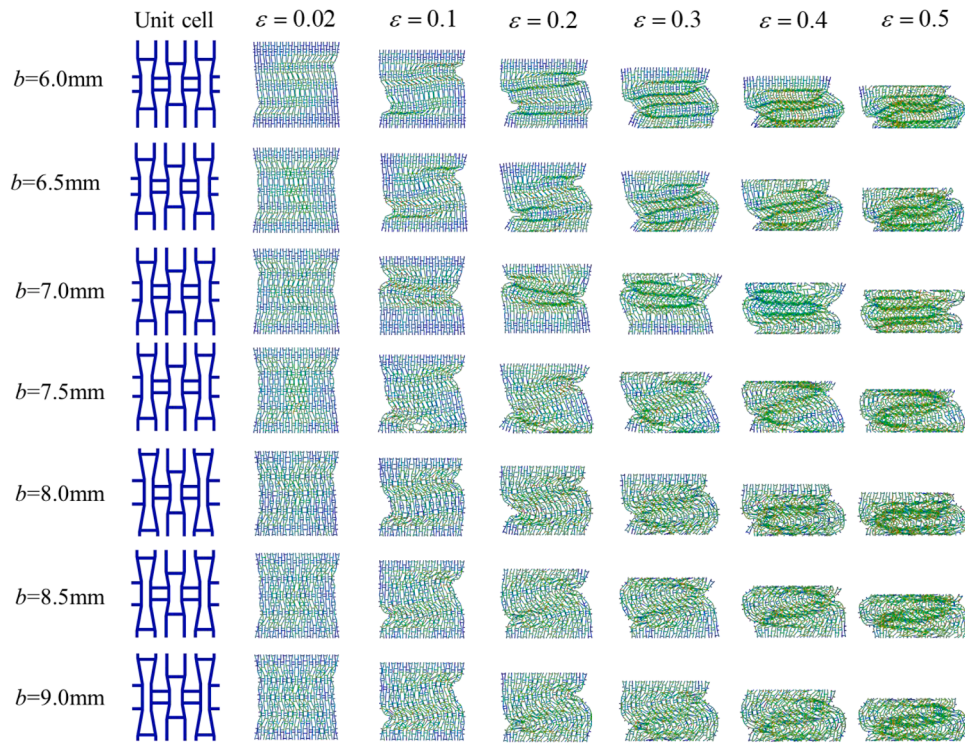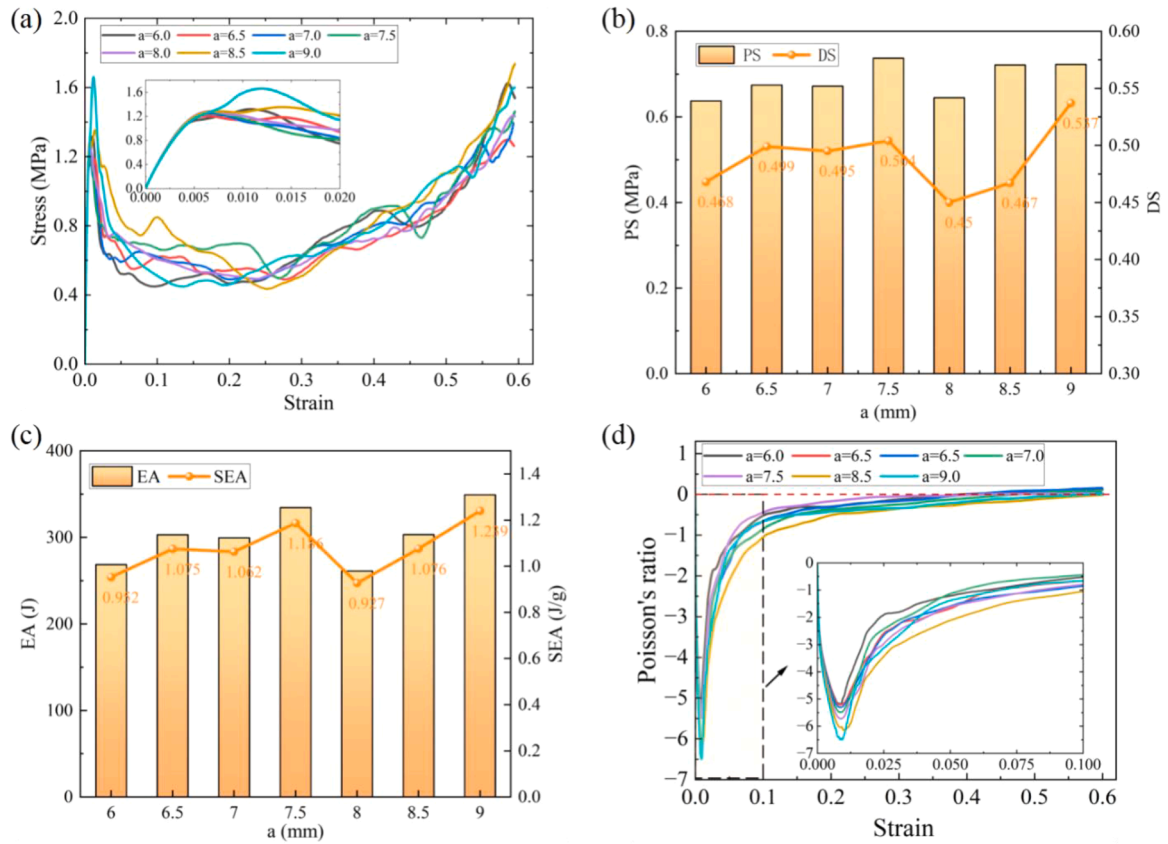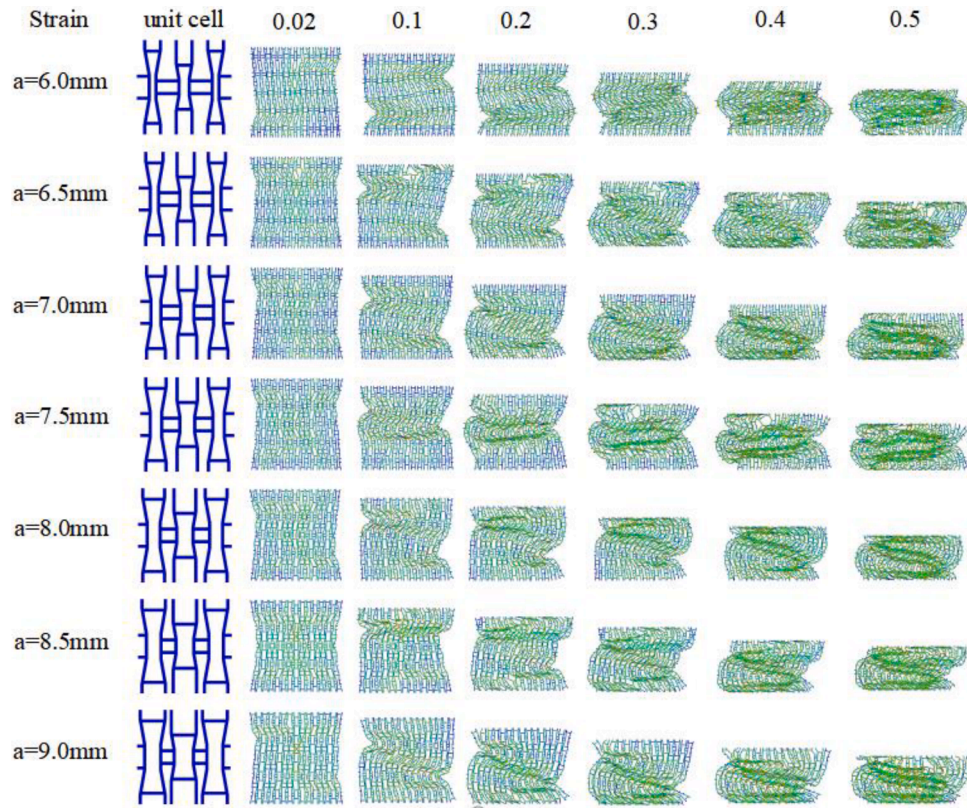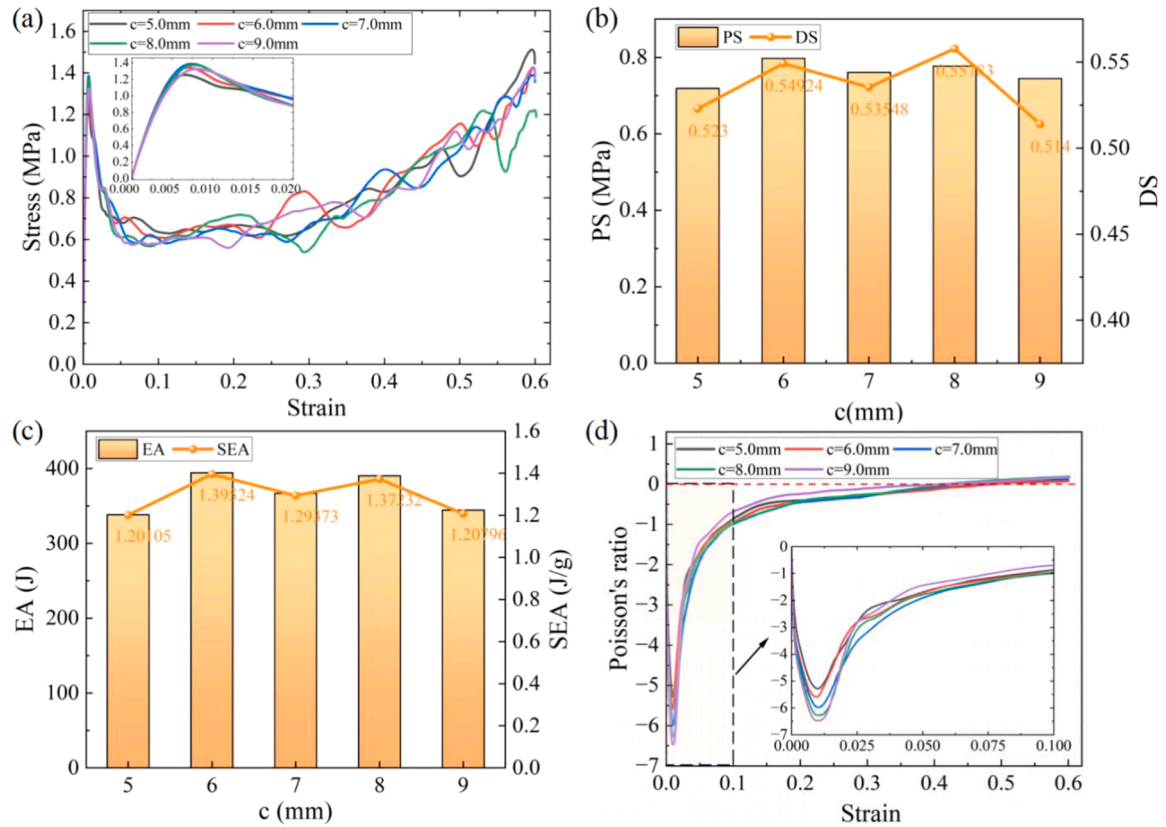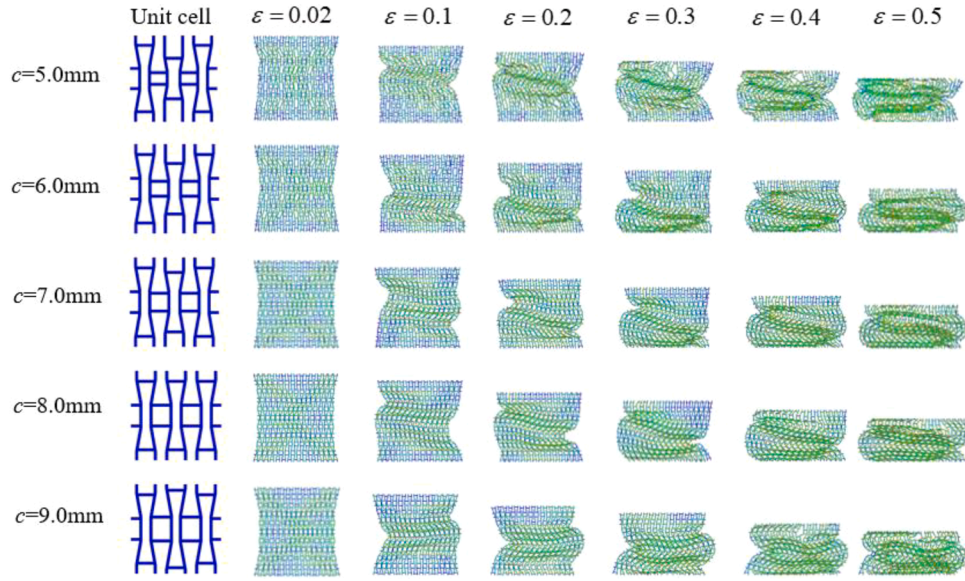
Fig. 22. The configuration of unit cell and deformation process of structures with different sub-structure height *c*.

reach the minimum negative Poisson's ratio increases. Fig. 22 illustrates the deformation process of structures with different sub-structure length. For $c = 5.0mm$ and $c = 6.0mm$, two shear bands appear in the middle of the structure at a strain of 0.2, and these bands gradually propagate throughout the structure as compression continues. For $c = 7.0$ mm, 8.0 mm, and 9.0 mm, no distinct shear bands are observed at a strain of 0.2, but two shear bands form at a strain of 0.3 and then propagate throughout the structure as compression continues.

4.3. Comparison with other researches

In this section, we compared the Poisson's ratio and the normalized Young's modulus along the principal axes with structures featuring enhanced auxeticity from recent studies [62–65]. As illustrated in Fig. 23 (a) and (b), similar to the Ashby material selection map, the Poisson's ratio and normalized Young's modulus are plotted as functions

of density. The existing structures exhibit negative Poisson's ratio ranging from 0 to -3, whereas the structure proposed in this study demonstrated lower values between -4 and -6, representing a 2 fold reduction compared to conventional configurations. The relative Young's modulus of these structures was calculated using Eq. (21). While other structures show relative Young's moduli in the range of 0–5, our proposed architecture achieves enhanced values of 7–20, corresponding to a 3- to 6-fold improvement over state-of-the-art structures. Fig. 23(c) presents the unit cell configurations of these structures. Theses unit cell configurations in existing studies are relatively simple, derived from re-entrant or star-shaped structures through combinations or modifications. In contrast, the structures in this study, obtained through topology optimization, are more complex.

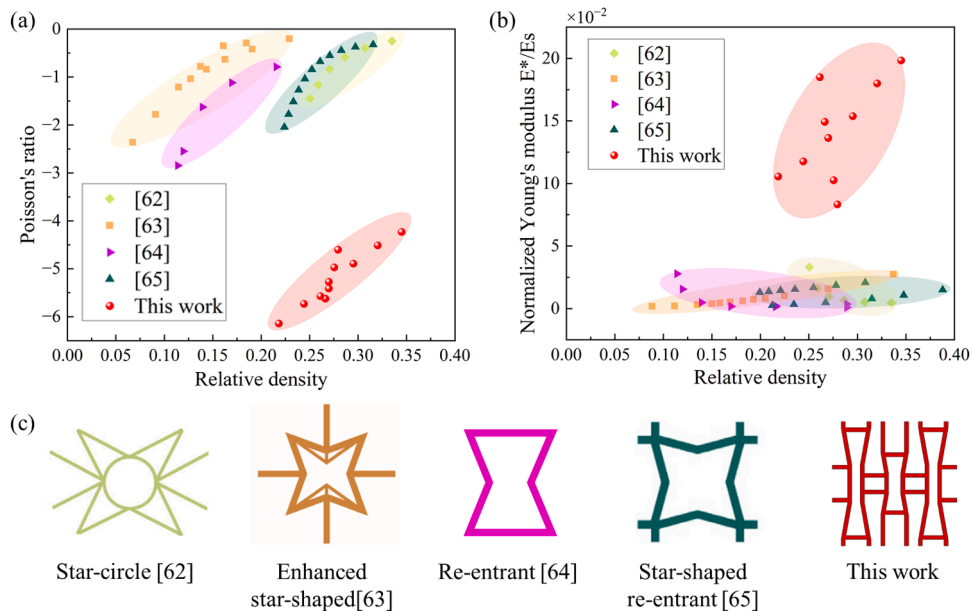$$\overline{E} = \frac{E^*}{E_S} \tag{21}$$

Fig. 23. Comparison of structures in this work and other studies related to enhanced auxeticity structures. (a) Comparison of the Poisson's ratios. (b) Comparison of the normalized Young's modulus. (c) Comparison of the unit cell configurations.

where $\bar{E}$ denotes relative Young's modulus, E^* is structural Young's modulus and E_S is the Young's modulus of the base material. The structural Young's modulus is the elastic modulus during elastic stage, and is calculated as:

$$E^* = \frac{\sigma_{IP}}{\varepsilon_{IP}} \tag{22}$$

where σ_{IP} represents the initial peak stress and ε_{IP} denotes the strain corresponding to the initial peak stress.

To further analyze the mechanisms behind the enhanced negative Poisson's ratio and high relative Young's modulus of the structure proposed in this paper, we compared the proposed structure with those found in other literature and discussed the enhancement mechanisms involved. For ASEA studied here, based on the deformation process illustrated in Fig. 12 and the Poisson's ratio and stress response shown in Fig. 13, it can be inferred that the enhanced negative Poisson's ratio effect is primarily associated with the re-entrant-like substructures on either side. Additionally, the lateral connecting rods of these substructures further contribute to this effect. The central substructure experiences minimal lateral contraction during compression, and creates an effective load transfer path between the upper and lower loading plates, which enhances the relative Young's modulus of the entire structure. In contrast, structures presented in references [62,63,65] achieve an enhanced negative Poisson's ratio effect through star-shaped configurations. These star structures can be seen as combinations of two re-entrant geometries along two axes; their concave features contribute to the enhanced negative Poisson's ratio effect. The Star-circle structure [62] integrates a central circle with slanted rods at both ends to enhance structural stiffness. The Enhanced star-shape structure [63] utilizes two star-shaped designs linked by four connecting rods to boost relative Young's modulus. Meanwhile, Star-shaped re-entrant structures [65] achieve greater structural stiffness by utilizing short rods at each corner to create stable substructures. While re-entrant design [64] are classic examples of negative Poisson's ratio structures, it will not be discussed further here. A summary of relevant findings is provided in Table 4.

5. Conclusion

In this paper, we employed topology optimization using the modified SIMP method and energy-based homogenization approach to obtain structural topology with negative Poisson's ratio characteristics. To mitigate the impact of local optimal solutions in topology optimization and to discover structures with enhanced auxeticity, we used multiple initial design domains and optimization parameters to conduct extensive topology optimization. 841 distinct structures exhibiting negative Poisson's ratio properties were generated. Among these, the structural topology with lowest negative Poisson's ratios was selected, and key structural parameters were identified for simplifications and further study. Experimental and finite element analysis were conducted to study the deformation modes, Poisson's ratio properties, and energy absorption of the structure. Furthermore, a parametric analysis was carried out to investigate the effects of cell wall thickness, cell wall angle, and substructure height on the structural properties. The key findings of this study are summarized as follows:

1. By using different initial design domains and optimization parameters, structures with enhanced auxeticity (less than -1) can be obtained.
2. The Poisson's ratio of the novel auxetic structure decreases continuously in the initial elastic phase, reaching a minimum value, and then increases rapidly, approaching zero at a strain of 0.6.
3. The larger the cell wall thickness (t), the higher the minimum Poisson's ratio, and the smaller the densification strain. When t=1.1 mm, the structure achieves the highest specific energy absorption (SEA).
4. Cell wall angle (α) affects the formation of shear bands in the structure. A larger α results in a higher minimum Poisson's ratio. The SEA is maximized when $\alpha = 82°$.
5. The sub-structure height (b) mainly influences the buckling modes of the structure, . Increasing b lowers the minimum Poisson's ratio, and the SEA is maximized when b=6 mm and 8.5 mm.
6. The larger the sub-structure width (a), the smaller the minimum Poisson's ratio. The specific energy absorption (SEA) of the structure is maximized when a=9 mm.

Table 4

Comparison of Poisson's ratio, relative Young's modulus and enhancement mechanism with other structures studied in other papers.

Reference	Type	Enhancement mechanism		Poisson's ratio	Relative Young's modulus(10^{-2})
		Poisson ratio	Relative Young's modulus		
This work	/	Two re-entrant-like substructures and lateral connecting rods	The central substructure creates an effective load transfer path	-0.32, -0.37, -0.44, -0.54, -0.67, -0.84, -1.03, -1.26, -1.51, -1.77, -2.04	8.333, 10.265, 10.557, 11.770, 13.635, 13.644, 14.932, 15.385, 18.001, 18.503, 19.838
Ref [62]	Star-circle	Star configuration	Central circle and slanted rods	-0.24, -0.39, -0.58,-0.83, -1.16,-1.44	0.443, 0.524, 0.667, 0.958, 1.623, 3.313
Ref [63]	Enhanced star-shape	Star configuration	Double star-shaped designs linked by four connecting rods	-0.20, -0.29, -0.34, -0.42, -0.63, -0.78, -0.84, -1.03, -1.21, -2.36, -1.78,	0.164, 0.203, 0.306, 0.385, 0.433, 0.518, 0.589, 0.719, 0.787, 1.026, 1.570, 2.748,
Ref [64]	Re-entrant	/	/	-0.79, -1.11, -1.63, -2.55, -2.84	0.0463, 0.0905, 0.148, 0.181, 0.226, 0.358, 0.484, 0.676 1.556
Ref [65]	Star-shaped re-entrant	Star configuration	Short rods at each corner	-0.32, -0.37, -0.44, -0.55, -0.67, -0.84, -1.04, -1.27, -1.51, -1.77, -2.04	0.260, 0.335, 0.482, 0.791, 1.073, 1.296, 1.357, 1.444, 1.506, 1.547, 1.680, 1.857 2.085

7. The larger the sub-structure height (c), the smaller the minimum Poisson's ratio. The SEA is maximized when c=6 mm.
8. The Poisson's ratio is 1–2 times smaller and the normalized Young's modulus is 3–6 times larger other structures in recent studies.

Future research could extend to 3D structures and explore more complex topologies. The novel auxetic structure can be further employed to develop sensors under small strain conditions due to the unique deformation amplification mechanism. The homogenization and topology optimization methods employed in this study are tailored for the linear elastic stage. Future research could utilize topology optimization that considers structural and material nonlinearities to consider deformation and stress responses of structures during large deformation stages. Meanwhile, research can be conducted on the energy absorption and damping capabilities of structures with different negative Poisson's ratios under impact loading, taking into account the mechanical characteristics of these structures at various strain rates.

Funding

Ethics approval and consent to participate

This study did not involve human or animal subjects, and thus, no ethical approval was required. The study protocol adhered to the guidelines established by the journal.

Replication of results

The data and methods used in this study are available for replication. Please contact the corresponding author for access to the necessary materials and detailed protocols.

CRediT authorship contribution statement

Kang Gao: Writing – original draft, Methodology, Investigation, Formal analysis, Conceptualization. **Zhiqiang Zou:** Validation, Resources. **Jiahui Liu:** Visualization, Validation. **Zeyang Li:** Writing – review & editing. **Zhangming Wu:** Writing – review & editing, Resources, Project administration, Funding acquisition.

Declaration of competing interest

The authors declare that they have no known competing financial interests or personal relationships that could have appeared to influence the work reported in this paper.

Acknowledgement

Data availability

Data will be made available on request.

Reference

[1] A.A. Zadpoor, Mechanical meta-materials, Mater. Horiz. 3 (2016) 371–381, https://doi.org/10.1039/C6MH00065G.

[2] D.M. Kochmann, K. Bertoldi, Exploiting microstructural instabilities in solids and structures: from metamaterials to structural transitions, Appl. Mech. Rev. 69 (2017), https://doi.org/10.1115/1.4037966.

[3] R. He, G. Schierning, K. Nielsch, Thermoelectric devices: A review of devices, architectures, and contact optimization, Adv. Mater. Technol. 3 (2018) 1700256, https://doi.org/10.1002/admt.201700256.

[4] X.-L. Peng, S. Bargmann, A novel hybrid-honeycomb structure: enhanced stiffness, tunable auxeticity and negative thermal expansion, Int. J. Mech. Sci. 190 (2021) 106021, https://doi.org/10.1016/j.ijmecsci.2020.106021.

[5] A. du Plessis, N. Razavi, M. Benedetti, S. Murchio, M. Leary, M. Watson, D. Bhate, F. Berto, Properties and applications of additively manufactured metallic cellular materials: A review, Prog. Mater. Sci. 125 (2022) 100918, https://doi.org/10.1016/j.pmatsci.2021.100918.

[6] Z. Zou, J. Liu, K. Gao, D. Chen, J. Yang, Z. Wu, Inverse design of functionally graded porous structures with target dynamic responses, Int. J. Mech. Sci. 280 (2024) 109530, https://doi.org/10.1016/j.ijmecsci.2024.109530.

[7] J.C. Ji, Q. Luo, K. Ye, Vibration control based metamaterials and origami structures: A state-of-the-art review, Mech. Syst. Signal Process. 161 (2021) 107945, https://doi.org/10.1016/j.ymssp.2021.107945.

[8] M. Gholikord, E. Etemadi, M. Imani, M. Hosseinabadi, H. Hu, Design and analysis of novel negative stiffness structures with significant energy absorption, thin-walled struct. 181 (2022) 110137. https://doi.org/10.1016/j.tws.2022.110137.

[9] M. Jia, N. Dai, T. Wang, Q. Cao, L. Yan, H. Dai, A compact quasi-zero stiffness metamaterial for energy absorption and impact protection, thin-walled struct. 205 (2024) 112360. https://doi.org/10.1016/j.tws.2024.112360.

[10] W. Zhou, Y. Li, J. Zhou, Y. Peng, Limb-inspired quasi-zero stiffness structure for ultralow-frequency vibration attenuation, Int. J. Mech. Sci. 274 (2024) 109251, https://doi.org/10.1016/j.ijmecsci.2024.109251.

[11] Q. Zhang, Y. Sun, A series of auxetic metamaterials with negative thermal expansion based on *L*-shaped microstructures, Thin-Walled Struct 197 (2024) 111596, https://doi.org/10.1016/j.tws.2024.111596.

[12] Q. Zhang, Y. Sun, Novel metamaterial structures with negative thermal expansion and tunable mechanical properties, Int. J. Mech. Sci. 261 (2024) 108692, https://doi.org/10.1016/j.ijmecsci.2023.108692.

[13] J. Huang, M. Fu, B. Zheng, A novel series of mechanical metamaterials with sign-changing coefficient of thermal expansion and their parameter analysis, Compos. Struct. 299 (2022) 116082, https://doi.org/10.1016/j.compstruct.2022.116082.

[14] Z. Xu, H. Zhao, K. Wang, Design of hourglass-lattice metastructure with near-zero thermal expansion using structural optimization method, Eng. Struct. 277 (2023) 115374, https://doi.org/10.1016/j.engstruct.2022.115374.

[15] R. Zeng, M. Xu, Y. Wang, J. Guo, R. Zhang, B. Yan, Z. Zhao, P. Wang, S. Duan, H. Lei, Three-dimensional bi-metallic lattice with multi-directional zero thermal expansion, Compos. Struct. 323 (2023) 117499, https://doi.org/10.1016/j.compstruct.2023.117499.

[16] B.J. Sahariah, M.J. Baishya, A. Namdeo, P. Khanikar, A novel strategy to design lattice structures with zero Poisson's ratio, Eng. Struct 288 (2023) 116214, https://doi.org/10.1016/j.engstruct.2023.116214.

[17] L. Rong, Z. Yifeng, Z. Yilin, C. Haiwen, C. Minfang, Three-dimensional orthogonal accordion cellular structures with multi-directional zero Poisson's ratio effects, Thin-Walled Struct 202 (2024) 112148, https://doi.org/10.1016/j.tws.2024.112148.

[18] X. Zhou, X. Liu, A. Zhao, C. Liu, H. Wu, Spatial tuning of the positive and negative Poisson's ratio of metamaterials through gradient design, Thin-Walled Struct 205 (2024) 112382, https://doi.org/10.1016/j.tws.2024.112382.

[19] J. Feng, Q. Liang, Y. Dou, J. He, Y. Wu, T. Chen, Higher stiffness hierarchical embedded strengthening honeycomb metastructure with small negative Poisson's ratio reduction, Thin-Walled Struct 179 (2022) 109561, https://doi.org/10.1016/j.tws.2022.109561.

[20] J. Tian, J. Yang, Y. Zhao, Metamaterial with synergistically controllable Poisson's ratio and thermal expansion coefficient, Int. J. Mech. Sci. 256 (2023) 108488, https://doi.org/10.1016/j.ijmecsci.2023.108488.

[21] L. Ren, X. Zhang, Z. Li, Y. Sun, Y. Tan, A novel negative Poisson's ratio structure with high Poisson's ratio and high compression resistance and its application in magnetostrictive sensors, Compos. Struct. 351 (2025) 118599, https://doi.org/10.1016/j.compstruct.2024.118599.

[22] J. Zhang, G. Lu, Z. You, Large deformation and energy absorption of additively manufactured auxetic materials and structures: A review, Compos. Part B Eng. 201 (2020) 108340, https://doi.org/10.1016/j.compositesb.2020.108340.

[23] J.B. Choi, R.S. Lakes, Fracture toughness of re-entrant foam materials with a negative Poisson's ratio: experiment and analysis, Int. J. Fract. 80 (1996) 73–83, https://doi.org/10.1007/BF00036481.

[24] R. Lakes, Advances in negative Poisson's ratio materials, Adv. Mater. 5 (1993) 293–296, https://doi.org/10.1002/adma.19930050416.

[25] M. Morvaridi, G. Carta, F. Bosia, A.S. Gliozzi, N.M. Pugno, D. Misseroni, M. Brun, Hierarchical auxetic and isotropic porous medium with extremely negative poisson's ratio, Extreme Mech. Lett. 48 (2021) 101405, https://doi.org/10.1016/j.eml.2021.101405.

[26] J. Zhang, M. Xiao, L. Gao, A. Alù, F. Wang, Self-bridging metamaterials surpassing the theoretical limit of Poisson's ratios, Nat. Commun. 14 (2023) 4041, https://doi.org/10.1038/s41467-023-39792-9.

[27] Z. Li, W. Gao, M.Yu Wang, C.H. Wang, Z. Luo, Three-dimensional metamaterials exhibiting extreme isotropy and negative Poisson's ratio, Int. J. Mech. Sci. 259 (2023) 108617, https://doi.org/10.1016/j.ijmecsci.2023.108617.

[28] B.M. Lempriere, Poisson's ratio in orthotropic materials, AIAA J 6 (1968) 2226–2227, https://doi.org/10.2514/3.4974.

[29] G.N. Greaves, A.L. Greer, R.S. Lakes, T. Rouxel, Poisson's ratio and modern materials, Nat. Mater. 10 (2011) 823–837, https://doi.org/10.1038/nmat3134.

[30] Y. Gao, Q. Wu, X. Wei, Z. Zhou, J. Xiong, Composite tree-like re-entrant structure with high stiffness and controllable elastic anisotropy, Int. J. Solids Struct. 206 (2020) 170–182, https://doi.org/10.1016/j.ijsolstr.2020.09.003.

[31] M. Chen, R. Zhong, Y. Wang, H. Wu, M. Fu, Mechanical properties of re-entrant chiral anisotropic honeycomb, Eng. Struct. 291 (2023) 116431, https://doi.org/10.1016/j.engstruct.2023.116431.

[32] A.M.M. Zamani, E. Etemadi, M. Bodaghi, H. Hu, Conceptual design and analysis of novel hybrid auxetic stents with superior expansion, Mech. Mater. 187 (2023) 104813, https://doi.org/10.1016/j.mechmat.2023.104813.

[33] A. Asadi, D. Hedayat, S. Ghofrani, A. Abouei Mehrizi, G. Shadalooyi, J. Kadkhodapour, A. Pourkamali Anaraki, Modification of hexachiral unit cell to enhance auxetic stent performance, Mech. Adv. Mater. Struct. 30 (2023) 1470–1484, https://doi.org/10.1080/15376494.2022.2034074.

[34] J. Liu, J. Liu, K. Gao, I. Mohagheghian, W. Fan, J. Yang, Z. Wu, A bioinspired gradient curved auxetic honeycombs with enhanced energy absorption, Int. J. Mech. Sci. 291–292 (2025) 110189, https://doi.org/10.1016/j.ijmecsci.2025.110189.

[35] A. Megdich, M. Habibi, L. Laperrière, Z. Li, Y. Abdin, Enhanced piezoelectric performance of PVDF/MWCNTs energy harvester through a 3D-printed multimodal auxetic structure for smart security systems, Mater. Today Sustain. 27 (2024) 100847, https://doi.org/10.1016/j.mtsust.2024.100847.

[36] A. Tabak, B. Safaei, A. Memarzadeh, S. Arman, C. Kizilors, An extensive review of piezoelectric energy-harvesting structures utilizing auxetic materials, J. Vib. Eng. Technol. 12 (2024) 3155–3192, https://doi.org/10.1007/s42417-023-01038-9.

[37] Y. Jiang, Z. Liu, N. Matsuhisa, D. Qi, W.R. Leow, H. Yang, J. Yu, G. Chen, Y. Liu, C. Wan, Z. Liu, X. Chen, Auxetic mechanical metamaterials to enhance sensitivity of stretchable strain sensors, Adv. Mater 30 (2018) 1706589, https://doi.org/10.1002/adma.201706589.

[38] M. Zhang, Y. Yang, H. Hu, S. Zhao, W. Song, N. Karim, H. Hu, High-performance stretchable strain sensors based on auxetic fabrics for human motion detection, ACS Appl. Mater. Interfaces 16 (2024) 49845–49855, https://doi.org/10.1021/acsami.4c13402.

[39] W. Wu, W. Hu, G. Qian, H. Liao, X. Xu, F. Berto, Mechanical design and multifunctional applications of chiral mechanical metamaterials: A review, Mater. Des. 180 (2019) 107950, https://doi.org/10.1016/j.matdes.2019.107950.

[40] G. Chen, Y. Cheng, P. Zhang, J. Liu, C. Chen, S. Cai, Design and modelling of auxetic double arrowhead honeycomb core sandwich panels for performance improvement under air blast loading, J. Sandw. Struct. Mater. 23 (2021) 3574–3605, https://doi.org/10.1177/1099636220935563.

[41] W. Liu, N. Wang, T. Luo, Z. Lin, In-plane dynamic crushing of re-entrant auxetic cellular structure, Mater. Des. 100 (2016) 84–91, https://doi.org/10.1016/j.matdes.2016.03.086.

[42] J.P. Lang, D. Han, X.G. Zhang, W. Jiang, Y. Zhang, X.H. Ni, J. Hao, X.C. Teng, X. Ren, A star-shaped tubular structure with multiple-directional auxetic effect, thin-walled struct. 193 (2023) 111247. https://doi.org/10.1016/j.tws.2023.111247.

[43] Q. Yang, Z. Li, H. Hao, W. Chen, Compressive mechanical properties and dynamic behaviour of origami-inspired tri-directional auxetic metastructure, Eng. Struct. 281 (2023) 115751, https://doi.org/10.1016/j.engstruct.2023.115751.

[44] J. Zhang, G. Lu, Z. Wang, D. Ruan, A. Alomarah, Y. Durandet, Large deformation of an auxetic structure in tension: experiments and finite element analysis, Compos. Struct. 184 (2018) 92–101, https://doi.org/10.1016/j.compstruct.2017.09.076.

[45] Z. Zhang, L. Zhang, Y. Dong, H. Chen, Y. Guo, Mechanical properties of negative poisson's ratio metamaterial units and honeycomb structures with cosine-like re-entrant structure, Mater. Lett. 331 (2023) 133451, https://doi.org/10.1016/j.matlet.2022.133451.

[46] H. Xu, H.-T. Liu, G.-F. Li, In-plane characteristics of a multi-arc re-entrant auxetic honeycomb with enhanced negative poisson's ratio effect and energy absorption, Eur. J. Mech. - ASolids 109 (2025) 105473, https://doi.org/10.1016/j.euromechsol.2024.105473.

[47] A. Alomarah, Y. Yuan, D. Ruan, A bio-inspired auxetic metamaterial with two plateau regimes: compressive properties and energy absorption, Thin-Walled Struct 192 (2023) 111175, https://doi.org/10.1016/j.tws.2023.111175.

[48] Q. Ma, H. Cheng, K.-I. Jang, H. Luan, K.-C. Hwang, J.A. Rogers, Y. Huang, Y. Zhang, A nonlinear mechanics model of bio-inspired hierarchical lattice materials consisting of horseshoe microstructures, J. Mech. Phys. Solids 90 (2016) 179–202, https://doi.org/10.1016/j.jmps.2016.02.012.

[49] Y. Zhang, M. Li, Z. Qi, R. Chen, Y. Lin, S. Cao, X. Li, R. Tang, H. Chen, Nonlinear mechanics of horseshoe microstructure-based lattice design, Int. J. Mech. Sci. 285 (2025) 109781, https://doi.org/10.1016/j.ijmecsci.2024.109781.

[50] Z. Chen, J. Li, B. Wu, X. Chen, X. Ren, Y.M. Xie, A novel bio-inspired helmet with auxetic lattice liners for mitigating traumatic brain injury, Smart Mater. Struct. 32 (2023) 105020, https://doi.org/10.1088/1361-665X/acf62e.

[51] H. Jiang, Y. Ren, Q. Jin, G. Zhu, Y. Hu, F. Cheng, Crashworthiness of novel concentric auxetic reentrant honeycomb with negative poisson's ratio biologically inspired by coconut palm, Thin-Walled Struct 154 (2020) 106911, https://doi.org/10.1016/j.tws.2020.106911.

[52] O. Sigmund, K. Maute, Topology optimization approaches: A comparative review, Struct. Multidiscip. Optim. 48 (2013) 1031–1055, https://doi.org/10.1007/s00158-013-0978-6.

[53] Y. Zheng, Y. Wang, X. Lu, Z. Liao, J. Qu, Evolutionary topology optimization for mechanical metamaterials with auxetic property, Int. J. Mech. Sci. 179 (2020) 105638, https://doi.org/10.1016/j.ijmecsci.2020.105638.

[54] A. Gupta, A. Gupta, R. Chowdhury, Computational design of auxetic microstructures via stress-based topology optimization, Eng. Struct. 319 (2024) 118807, https://doi.org/10.1016/j.engstruct.2024.118807.

[55] M. Ye, L. Gao, H. Li, A design framework for gradually stiffer mechanical metamaterial induced by negative Poisson's ratio property, Mater. Des. 192 (2020) 108751, https://doi.org/10.1016/j.matdes.2020.108751.

[56] M. Ye, H. Li, X. Cai, L. Gao, A. Zhang, Z. Zhao, Progressive design of gradually stiffer metamaterial using surrogate model, Compos. Struct. 264 (2021) 113715, https://doi.org/10.1016/j.compstruct.2021.113715.

[57] L. Xia, P. Breitkopf, Design of materials using topology optimization and energy-based homogenization approach in Matlab, Struct. Multidiscip. Optim. 52 (2015) 1229–1241, https://doi.org/10.1007/s00158-015-1294-0.

[58] O. Sigmund, Materials with prescribed constitutive parameters: an inverse homogenization problem, Int. J. Solids Struct. 31 (1994) 2313–2329, https://doi.org/10.1016/0020-7683(94)90154-6.

[59] M.P. Bendsøe, O. Sigmund, Material interpolation schemes in topology optimization, Arch. Appl. Mech. 69 (1999) 635–654, https://doi.org/10.1007/s004190050248.

[60] Y. Zhang, M. Xiao, H. Li, L. Gao, Topology optimization of material microstructures using energy-based homogenization method under specified initial material layout, J. Mech. Sci. Technol. (2019).

[61] X. Niu, F. Xu, Z. Zou, T. Fang, S. Zhang, Q. Xie, In-plane dynamic crashing behavior and energy absorption of novel bionic honeycomb structures, Compos. Struct. 299 (2022) 116064, https://doi.org/10.1016/j.compstruct.2022.116064.

[62] H. Lu, X. Wang, T. Chen, Enhanced stiffness characteristic and anisotropic quasi-static compression properties of a negative poisson's ratio mechanical metamaterial, Thin-Walled Struct 179 (2022) 109757, https://doi.org/10.1016/j.tws.2022.109757.

[63] N. Xu, H.-T. Liu, M.-R. An, L. Wang, Novel 2D star-shaped honeycombs with enhanced effective young's modulus and negative poisson's ratio, Extreme Mech. Lett. 43 (2021) 101164, https://doi.org/10.1016/j.eml.2020.101164.

[64] K. Khorshidi, M. Rezaeisaray, M. Karimi, Energy harvesting using vibrating honeycomb sandwich panels with auxetic core and carbon nanotube-reinforced face sheets, Int. J. Solids Struct. 256 (2022) 111988, https://doi.org/10.1016/j.ijsolstr.2022.111988.

[65] L. Ai, X.-L. Gao, An analytical model for star-shaped re-entrant lattice structures with the orthotropic symmetry and negative poisson's ratios, Int. J. Mech. Sci. 145 (2018) 158–170, https://doi.org/10.1016/j.ijmecsci.2018.06.027.